

# Multivariate Median Filters and Partial Differential Equations

Martin Welk

University for Health Sciences, Medical Informatics and Technology (UMIT),  
Eduard-Wallnöfer-Zentrum 1, 6060 Hall/Tyrol, Austria  
`martin.welk@umit.at`

March 18, 2015

## Abstract

Multivariate median filters have been proposed as generalisations of the well-established median filter for grey-value images to multi-channel images. As multivariate median, most of the recent approaches use the  $L^1$  median, i.e. the minimiser of an objective function that is the sum of distances to all input points. Many properties of univariate median filters generalise to such a filter. However, the famous result by Guichard and Morel about approximation of the mean curvature motion PDE by median filtering does not have a comparably simple counterpart for  $L^1$  multivariate median filtering. We discuss the affine equivariant Oja median and the affine equivariant transformation–retransformation  $L^1$  median as alternatives to  $L^1$  median filtering. We analyse multivariate median filters in a space-continuous setting, including the formulation of a space-continuous version of the transformation–retransformation  $L^1$  median, and derive PDEs approximated by these filters in the cases of bivariate planar images, three-channel volume images and three-channel planar images. The PDEs for the affine equivariant filters can be interpreted geometrically as combinations of a diffusion and a principal-component-wise curvature motion contribution with a cross-effect term based on torsions of principal components. Numerical experiments are presented that demonstrate the validity of the approximation results.

**Keywords:** Median filtering • Affine equivariance • Oja median • Multi-channel images  
• Transformation–retransformation median • Curvature-based PDE

## 1 Introduction

Median filtering of signals and images goes back to the work of Tukey [27] and has since then been established in image processing as a simple nonlinear denoising method for grey-value images with the capability to denoise even impulse noise and similar types of noise with heavy-tailed distributions, and to retain at the same time sharp edges in the denoising process.

Like other local image filters, the median filter consists of a *selection step* that identifies for each pixel location those pixels which will enter the computation of the filtered value at that location, followed by an *aggregation step* that combines the intensities of these pixels into the filtered value. In the standard setting, the selection step uses a fixed-shape sliding window, which can be called the *structuring element* following the naming convention from mathematical morphology. The aggregation step consists in taking the median of the selected intensities. The process can be iterated, giving rise to what is called the *iterated median filter*.

The median filter, particularly in its iterated form, has been subject to intensive investigation over the decades. For example, [13] studied so-called *root signals*, non-trivial steady states that occur in the iterated median filter and depend subtly on the choice of the structuring element. Work by Guichard and Morel [15] has identified iterated median filtering as an explicit nonstandard discretisation of (mean) curvature motion [2], thus establishing a link between the discrete filter concept and a partial differential equation (PDE).

**Multivariate median filtering.** Given the merit of median filtering in processing grey-value images one is interested in stating also a median filter for multi-channel images such as colour images, flow fields, tensor fields etc. As the switch from single- to multi-channel images does not affect the selection step mentioned above but solely the aggregation, it is clear that what is needed to accomplish this goal is the definition of a multivariate median.

A straightforward approach to median filtering of multi-channel data is to establish some kind of linear order in  $\mathbb{R}^n$ . For example, [9] considered a vector median filter of this type (based on lexicographic ordering) and derived even PDEs for this filter. A clear shortcoming of such an approach, however, is that mapping  $\mathbb{R}^n$  to  $\mathbb{R}$  (which necessarily happens with a linear order) either breaks injectivity or continuity, and is usually incompatible with natural geometric invariances of the data colour space, like symmetries of colour spaces, or the Euclidean or affine structures of flow vectors or tensor spaces.

A starting point for a multivariate median definition that avoids these problems is the following characterisation of the univariate median: A median of a tuple  $\mathcal{X} = (x_1, \dots, x_N)$  of real numbers  $x_1, \dots, x_N$  is a real number that minimises the sum of distances to all numbers of the set,

$$m(\mathcal{X}) = \operatorname{argmin}_{x \in \mathbb{R}} \sum_{i=1}^N |x - x_i|. \quad (1)$$

Strictly speaking, this minimiser is unique only if the data set is of odd cardinality; for even-numbered input sets, the two middle elements in the rank order and all real numbers in between fulfil the criterion, making  $\operatorname{argmin}$  actually set-valued. Heuristics like mean value are often used to disambiguate the median in this situation. We will not consider this here but keep in mind that there is a whole set of medians in this case. At any rate, in the univariate case, there happens to always exist a number from the given data set which is a median of this set, such that one can also write

$$m(\mathcal{X}) = \operatorname{argmin}_{x \in \mathcal{X}} \sum_{i=1}^N |x - x_i|. \quad (2)$$

Early attempts to multi-channel median filtering in the computer science and signal processing literature, starting from [4] in 1990, defined therefore a vector-valued “median” that selects *from the set of input points* in  $\mathbb{R}^n$  the one that minimises the sum of distances to all other sample points. Given a tuple  $\mathcal{X} := (\mathbf{x}_1, \dots, \mathbf{x}_N)$  of points  $\mathbf{x}_i \in \mathbb{R}^n$ , this amounts to

$$\mathbf{m}_{L^1|\mathcal{X}}(\mathcal{X}) := \operatorname{argmin}_{\mathbf{x} \in \mathcal{X}} \sum_{i=1}^N \|\mathbf{x} - \mathbf{x}_i\|. \quad (3)$$

In a more differentiating terminology, see e.g. [26], such a concept would rather be called a *medoid*.

More recent approaches, such as [19, 25] for colour images or [35] for symmetric matrices, rely on the same minimisation but without the restriction to the given data points, i.e. (in the same notations as before)

$$\mathbf{m}_{L^1}(\mathcal{X}) := \operatorname{argmin}_{\mathbf{x} \in \mathbb{R}^n} \sum_{i=1}^N \|\mathbf{x} - \mathbf{x}_i\|. \quad (4)$$

The underlying multivariate median concept can be traced back in the statistics literature to works by Hayford from 1902 [16] and Weber from 1909 [29], followed by [5, 14, 30] and many others. It is nowadays denoted as the *spatial median* or  *$L^1$  median*. The  $L^1$  median is unique for all non-collinear input data sets. Only for collinear sets non-uniqueness as for the univariate median takes place; in this case, the argmin in (4) is actually set-valued. As these configurations are non-generic, we do not follow this issue further. For the computation of  $L^1$  medians, efficient algorithms are available, see e.g. [28].

However, the  $L^1$  median is not the only multivariate median concept in literature. Another generalisation of the same minimisation property of the univariate median was introduced by Oja in 1983 [21] and is known as the *simplex median* or *Oja median*. Here, distances between points on the real line from the univariate median definition are generalised not to distances in  $\mathbb{R}^n$  but to simplex volumes. Thus, the simplex median of a finite set of points in  $\mathbb{R}^n$  is the point  $\mathbf{m} \in \mathbb{R}^n$  that minimises the sum of simplex volumes  $||[\mathbf{m}, \mathbf{a}_1, \dots, \mathbf{a}_n]||$  where  $\mathbf{a}_i$  are distinct points of the input data set, i.e.

$$\mathbf{m}_{\text{Oja}}(\mathcal{X}) := \operatorname{argmin}_{\mathbf{x} \in \mathbb{R}^n} \sum_{1 \leq i_1 < \dots < i_n \leq N} ||[\mathbf{x}, \mathbf{x}_{i_1}, \dots, \mathbf{x}_{i_n}]||. \quad (5)$$

An advantage of this concept that is relevant for many statistics applications is its affine equivariance, i.e. that it commutes with affine transformations of the data space. In contrast, the  $L^1$  median only affords Euclidean equivariance. It should be noticed that also in an image processing context affine equivariance offers an advantage over just Euclidean equivariance: For images whose value ranges are not equipped with a meaningful Euclidean structure, justification of Euclidean equivariant concepts like the  $L^1$  median is questionable.

While there exist in any dimension even datasets that are not degenerated to hyperplanes whose Oja median is non-unique, these cases are non-generic. A more substantial caveat is that the Oja median is always undefined when the input data lie on a common hyperplane. Heuristics exist to cure this but usually these interfere with affine equivariance.

Whereas the affine equivariance of the Oja median concept has been welcomed in the statistical community, its computational complexity was considered a problem from the beginning, see the discussion in Section 2.1. On one hand, there are some results regarding more efficient computation of Oja medians, see e.g. [1, 23]. On the other hand, researchers have been inspired soon to design multivariate median concepts that combine affine equivariance with the efficiency of the  $L^1$  median [10, 17, 22], see also the survey in [11]. In these approaches, affine equivariance is achieved using a *transformation-retransformation* method. Input data sets are normalised by a data-dependent affine transform  $\mathbf{T}_{\mathcal{X}} : \mathbb{R}^n \rightarrow \mathbb{R}^n$ . Applying the standard  $L^1$  median and transforming back to the original data space then yields an affine equivariant median operation

$$\mathbf{m}_{L^1; \text{aff}}(\mathcal{X}) := \mathbf{T}_{\mathcal{X}}^{-1}(\mathbf{m}_{L^1}(\mathbf{T}_{\mathcal{X}}(\mathcal{X}))) = \mathbf{T}_{\mathcal{X}}^{-1} \left( \operatorname{argmin}_{\mathbf{y} \in \mathbb{R}^n} \sum_{i=1}^N \|\mathbf{y} - \mathbf{T}_{\mathcal{X}}(\mathbf{x}_i)\| \right). \quad (6)$$

The data-dependent affine transform in these approaches is typically based on an estimator of the covariance matrix of the distribution underlying the observed data, such that the transformed data are supposed to follow an isotropic distribution.

Besides these multivariate median concepts that generalise in different ways the distance sum minimisation property of the univariate median, there exist several other concepts which we will not consider here, see the review [24].

**Multivariate median filters and PDE.** While the above-mentioned relationship between univariate median filtering and the mean curvature motion PDE could be extended to relate also adaptive median filtering procedures [34] and further discrete filters [33] to well-understood PDEs of image processing, the picture changes when turning to multivariate median filtering. As demonstrated in [33], it is possible to derive some PDE for median filtering based on the spatial median as in [25]. However, this PDE involves complicated coefficient functions coming from elliptic integrals most of which cannot even be stated in closed form, see [33] and for the bivariate case [31]. During the present work it became evident that the analysis of the  $L^1$  median filter in [33] contained a mistake with the consequence that one term was omitted in the resulting PDE. We will state in the present paper corrected results for the case of two- and three-channel data, the latter restricted to a relevant special case. A corrected result for the general multivariate case with proof will be provided in a forthcoming technical report [32].

Given the unfavourable complexity of the PDE approximated by  $L^1$  median filtering, the question arises whether other multivariate median concepts could be advantageous in multi-channel image processing. The paper [31] was intended as a first step in this direction which is continued in the present contribution. Whereas in [31] only bivariate images over planar domains (like 2D flow fields or, somewhat artificial, two-colour images) were covered, we extend the view here to include three-channel volume images (like 3D flow fields) and three-channel planar images (like colour images). Moreover, we include also an affine equivariant transformed  $L^1$  median filter based on the transformation–retransformation procedure in our analysis.

**Our contribution.** This paper extends the work from [31]. Regarding bivariate median filtering of planar images, we restate in this paper the PDE approximation result for the Oja median from [31]. We present its proof from [31] in a slightly modified and more detailed form, and present a new, alternative proof. We compare the PDE with that for bivariate  $L^1$  median filtering and discuss the geometric meaning of these PDEs, showing that they combine an isotropic diffusion contribution with a curvature motion part and torsion-based cross-effects between the channels. We also discuss the degeneracy of the PDE approximated by the Oja median when the Jacobian of the input function becomes singular. We also give a formulation for a space-continuous version of the transformation–retransformation median, which enables us, by recombining ideas from the analysis of the  $L^1$  and Oja median filters, to derive a PDE approximation statement for this filter. The outcome is that the two affine equivariant medians, Oja median and transformation–retransformation  $L^1$  median, are asymptotically equivalent as image filters in the case of bivariate planar images.

In the case of three-channel volume images, we prove PDE approximation results for the Oja median and transformation–retransformation  $L^1$  median. The PDE is again identical

for both filters, implying their asymptotical equivalence. Its structure is analogous to the bivariate case, with the diffusion, mean curvature motion and torsion-based cross-effect terms.

For three-channel planar images, for which the 3D Oja median on local neighbourhoods is degenerated or almost degenerated, we compare the 2D Oja median (minimiser of sum of triangle areas) applied to 3D data with the transformation–retransformation  $L^1$  median, and derive PDE approximation results for both, which again display the same structure as in the cases before and confirm asymptotical equivalence of the two filters.

We test, and verify to reasonable accuracy, the PDE approximations in all dimensional settings by numerical experiments that compare discrete multivariate median filters for example functions sampled at high grid resolutions with theoretically derived PDE time steps. Finally, we investigate iterated Oja and transformation–retransformation  $L^1$  median filtering of RGB colour images and compare it to a numerical evaluation of the corresponding PDE. These experiments, too, confirm the theoretical results.

**Structure of the paper.** The remainder of the paper is structured as follows. In Section 2, we demonstrate two- and three-channel median filters on a 2D flow field, as a bivariate test case, and RGB colour images, as a three-channel example. For the latter, we consider four variants of three-channel medians:  $L^1$ , 2D Oja, 3D Oja and transformation–retransformation  $L^1$  median. Finally, we discuss basic geometric properties of the  $L^1$  and Oja medians in the bivariate setting. Section 3 is dedicated to the analysis of multivariate median filters for bivariate planar images, three-channel volume images and three-channel planar images. PDE approximation results generalising Guichard and Morel’s [15] result for the univariate case are derived in all settings, and discussed. In Section 4 the results of the theoretical analysis are validated by numerical experiments on analytic example functions and RGB images, where the latter also cover iterated median filtering. A summary and outlook is given in Section 5. Appendices A–E contain detailed proofs for lemmas from Section 3. Appendix F details a finite-difference scheme for the PDE approximated by affine equivariant median filters for RGB images that is used for the experiments in Section 4.

## 2 Comparison of $L^1$ and Oja Median

To motivate our theoretical analysis, we will demonstrate in this section the effects of image filters based on the  $L^1$  and Oja median by experiments on image and flow field data. Additionally, some geometric intuition about the  $L^1$  and Oja medians in the bivariate case will be given to help understanding their relations.

### 2.1 Numerical Realisation of Multivariate Median Filters

Before we turn to presenting filtering experiments, some words need to be said about the implementations of the filters as they are used in this paper. Given the focus of this work at theoretical connections, simplicity and comparability of the implementations are in the foreground. Computational efficiency is not a goal, thus possibilities for improvements in this respect are only touched grazingly.

Since the objective functions of the  $L^1$  and Oja medians are convex, one can think of numerous generic minimisation algorithms. However, the objective functions are only piecewise smooth, and may be extremely anisotropic around their minima. This poses difficulties for

algorithms. For the numerical computation of  $L^1$  and Oja medians in this work, we use therefore a gradient descent approach with adaptive step-size control using a line search, similar to the proceeding described in [35]. The advantage of this approach is its simplicity and the fact that it can be used in a straightforward way for all median variants considered in this work.

For the  $L^1$  median  $\mathbf{m}_{L^1}(\mathcal{X})$ , one reads off (4) the objective function  $f(\mathbf{x}) = \sum_{i=1}^N \|\mathbf{x} - \mathbf{x}_i\|$ . Its gradients are computed directly by summation over the data points, which has a linear complexity  $\mathcal{O}(N)$ , which is fast enough to filter e.g.  $512 \times 512$  images with structuring elements of radius 5 within less than 3 minutes in single-threaded CPU computation on a 3 GHz machine. A substantially more efficient computation would be possible by using an iterative weighted means algorithm for the  $L^1$  median, see [28].

For Oja medians  $\mathbf{m}_{\text{Oja}}(\mathcal{X})$  of two- and three-dimensional input data, see (5), the objective functions are sums of triangle areas,  $f(\mathbf{x}) = \sum_{1 \leq i < j \leq N} |[\mathbf{x}, \mathbf{x}_i, \mathbf{x}_j]|$ , or tetrahedron volumes,  $f(\mathbf{x}) = \sum_{1 \leq i < j < k \leq N} |[\mathbf{x}, \mathbf{x}_i, \mathbf{x}_j, \mathbf{x}_k]|$ , respectively. Their gradients are computed here by summation over pairs or triples, respectively, of data points, which amounts to an  $\mathcal{O}(N^2)$  or  $\mathcal{O}(N^3)$  complexity, respectively, and is therefore computationally expensive. It is possible in this way to compute two- and three-dimensional Oja medians of test functions within sampled structuring elements and image filters based on two-dimensional Oja medians, with computation times ranging from minutes to hours in single-threaded CPU computation, depending on image and structuring element sizes, and numerical convergence criteria for the gradient descent. The convergence of the gradient descent computation can be somewhat accelerated if the input data are subjected to an affine transformation that makes their distribution more isotropic, which is possible based on the affine equivariance of the Oja median. Principal axis transform of the covariance matrix can be used to determine a suitable transformation.

In practical application contexts, the computational expense of such an Oja median filter would be unacceptable. Let us therefore mention possible alternatives. For the bivariate case, [1] describes an algorithm that allows to compute two-dimensional Oja medians in  $\mathcal{O}(N \log^3 N)$  time. This is achieved by an angular reordering of points in the gradient computation together with geometric considerations that limit the possible locations for Oja medians to a small set of discrete points in the plane. It can be expected that using this algorithm would speed up an image filter with a structuring element of radius 5 (approx. 80 sample points) by two to three orders of magnitude. Highly parallel computation such as on GPUs would further improve on this.

For Oja medians in general dimensions, we refer to [23] where several exact and stochastic algorithms are discussed.

An additional difficulty with Oja medians specifically in image filtering results from the frequent occurrence of degenerated input data. In a multivariate image, data vectors belonging to pixels from a small local neighbourhood will often concentrate around or even lie on a lower-dimensional submanifold of the actual data space. In such a case, the objective function of the Oja median is made up by volumes of degenerated or almost degenerated simplices, and the filtering result becomes undetermined or numerically unstable.

One simple, albeit expensive, way to cope with these degeneracies of Oja medians is to replace each input data point with a set of data points that are isotropically scattered in a small neighbourhood of the actual input point. Thereby one enforces the full dimensionality of the input set, thus the input data are regularised. Note, however, that the isotropic scattering of the new data points involves a notion of metric, and thus goes at the cost of



Figure 1: Frame 5 from the *Hamburg taxi sequence* (author: H.-H. Nagel), size:  $256 \times 190$  pixels.

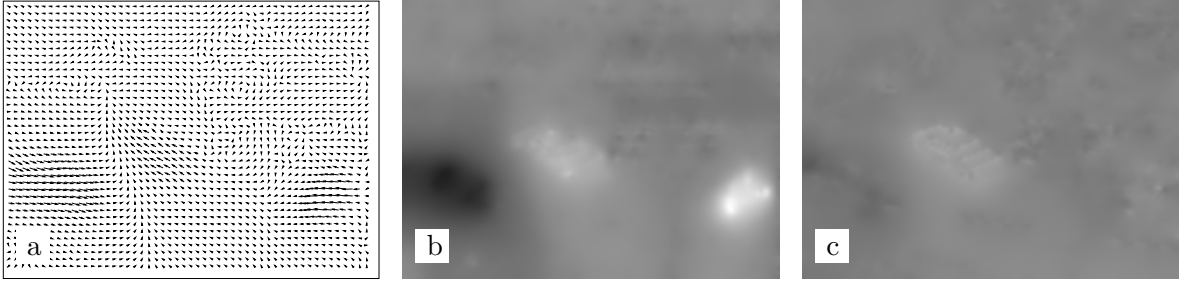


Figure 2: Optical flow between Frames 5 and 6 of the Hamburg taxi sequence, computed by a coarse-to-fine Horn-Schunck method with warping. Magnitudes of vector entries range up to approx. 2.44. **(a)** Flow field visualised by vector arrows, subsampled (every 5th flow vector in  $x$  and  $y$  direction is shown). – **(b)** Horizontal component of the same flow field. Grey (128) represents zero, brighter values represent flows to the left, darker values flows to the right. – **(c)** Vertical component of the flow field. Grey represents zero, brighter values represent upward flows, darker values downward flows.

affine equivariance. In our experiment series with Oja median filtering on one test image (shown in Figure 5 in Section 2.3 and used again in Figure 9 in Section 4.2) we perform this kind of input regularisation by replacing each input point by the corners of a regular simplex centered at the input point, along with the above-mentioned principal axis transform. All other Oja median experiments are done with the plain gradient descent algorithm without these modifications.

To complement the standard  $L^1$  median and Oja median filters, we want to perform also filtering based on the affine equivariant transformed  $L^1$  median (6). The affine transform  $\mathbf{T}_{\mathcal{X}}$  for a tuple  $\mathcal{X}$  of input data is computed from the same principal axis transform of the covariance matrix as mentioned above in such a way that the covariance matrix for the transformed data  $\mathbf{T}_{\mathcal{X}}(\mathcal{X})$  becomes diagonal, with the diagonal entries being 1 in most cases. Only if the original covariance matrix is singular or almost singular, some of the diagonal entries will be close or equal to 0. The  $L^1$  median  $\mathbf{m}_{L^1}$  inside (6) is computed by our gradient descent method.

## 2.2 Median Filtering of 2D Flow Fields

We turn first to the bivariate case. Possible applications for this setup include two-channel colour images, for which an example was presented in [31], or, with more practical relevance, 2D flow fields.

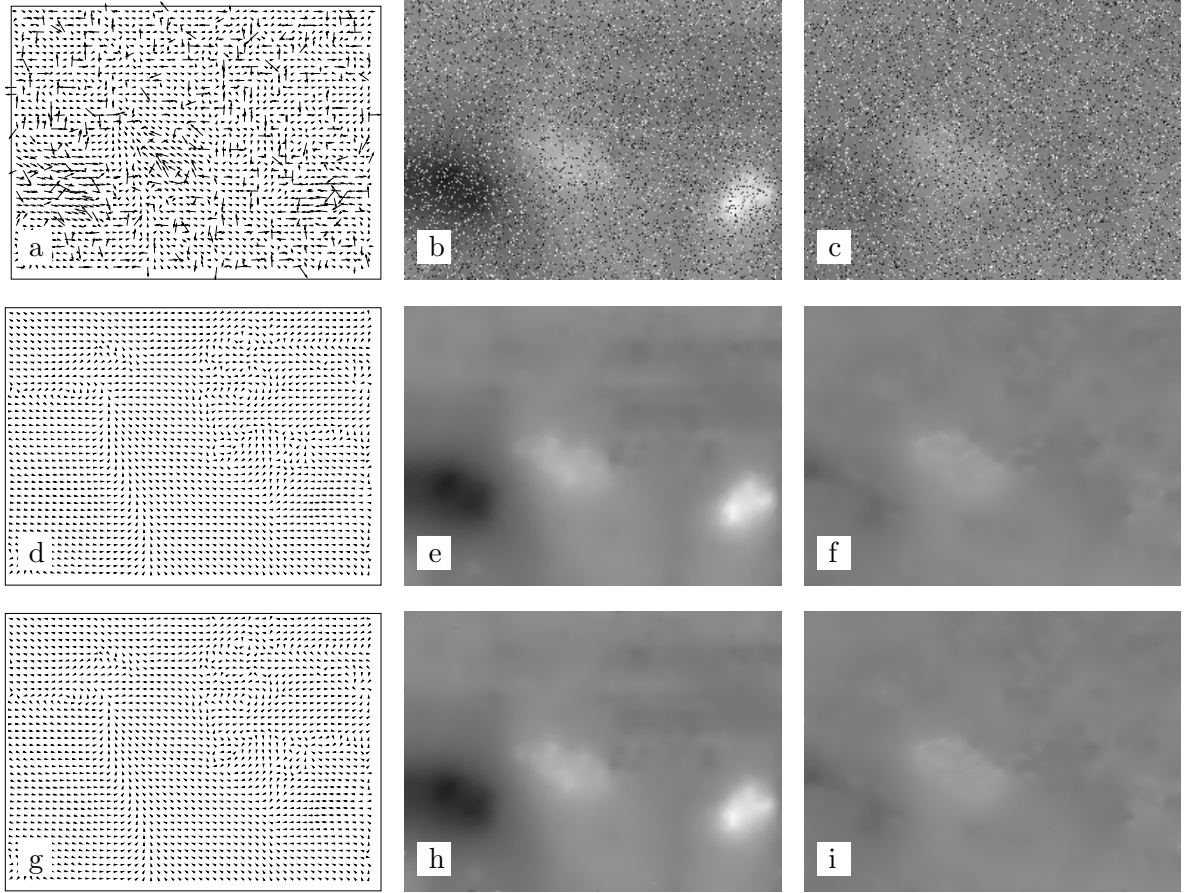


Figure 3: **Top row:** Flow field from Figure 2 degraded by uniform noise where 20 % of the vector entries have been replaced by random values in  $[-2.44, 2.44]$ . **(a)** Subsampled vector field representation. – **(b)** Horizontal component. – **(c)** Vertical component. – **Middle row (d–f):** Denoised by one step of  $L^1$  median filtering with a disc-shaped structuring element of radius 3. **Bottom row (g–i):** Denoised by one step of Oja median filtering with the same structuring element as in (d–f).

We demonstrate here bivariate median filtering on an exemplary flow field computed from two frames of the *Hamburg taxi sequence*. The first of these frames is shown in Figure 1. Within the sequence, the taxi moves in the upper left direction, whereas two vehicles enter the scene from the left and right margin. The flow field, visualised in Figure 2, has been obtained using an implementation of the Horn-Schunck method [18] within a coarse-to-fine multiscale approach with warping [3, 20] in order to cope with displacements larger than one pixel.

In the top row of Figure 3 this flow field has been degraded by uniform impulse noise with 20 % density applied to the horizontal and vertical flow components independently. The middle and bottom row of Figure 3 show results of  $L^1$  and Oja median filtering, respectively, both of which succeed to remove the noise and restore a smooth flow field similar to the original one. Note that the filtering results of both median filters are very similar.

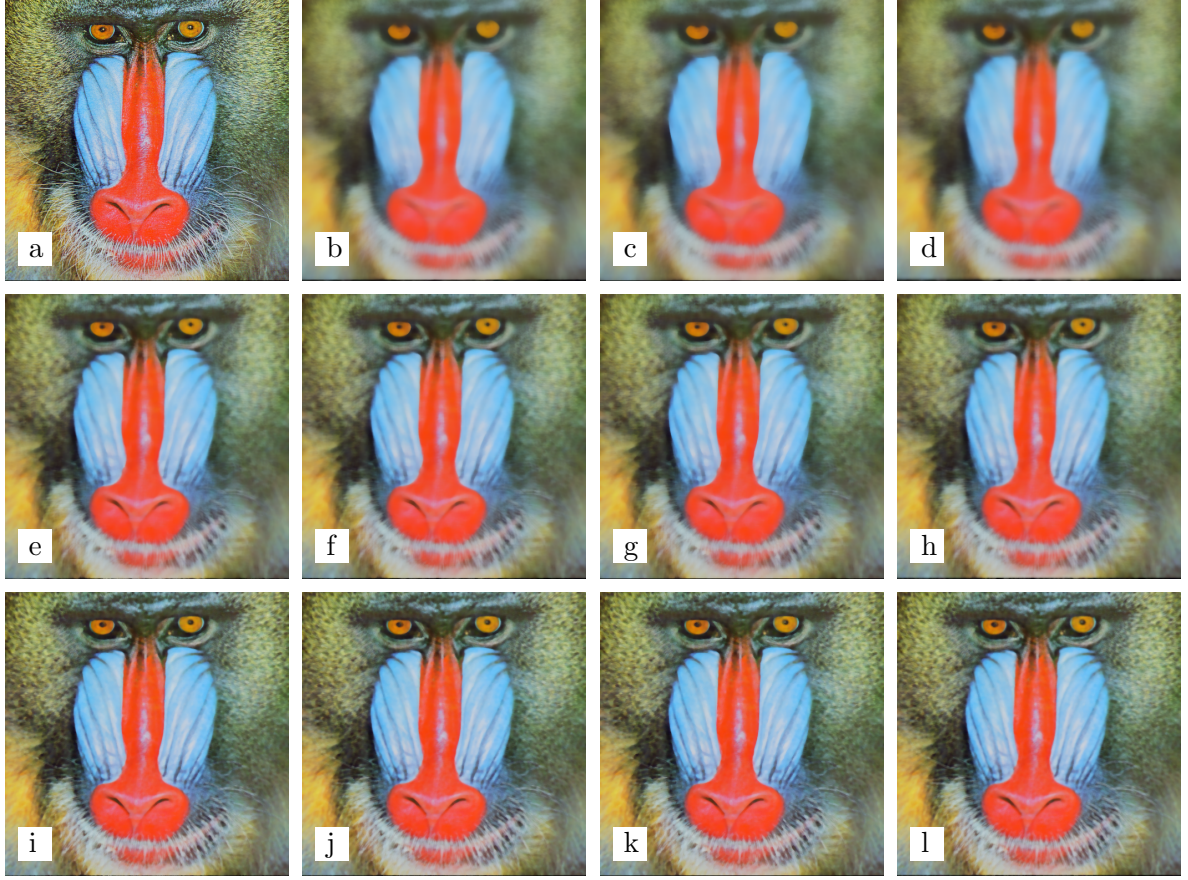


Figure 4: Median filtering of the *Baboon* test image using different multivariate medians and disc-shaped structuring elements  $D_\varrho$  of varying radius. **Top row, left to right:** (a) Original RGB image ( $512 \times 512$  pixels). – (b) Filtered using 2D Oja median with  $\varrho = 10$ . – (c) Filtered using  $L^1$  median with  $\varrho = 10$ . – (d) Filtered using affine equivariant transformed  $L^1$  median with  $\varrho = 10$ . – **Middle row, left to right:** (e) Filtered using 3D Oja median with  $\varrho = 5$ . – (f) Filtered using 2D Oja median with  $\varrho = 5$ . – (g) Filtered using  $L^1$  median with  $\varrho = 5$ . – (h) Filtered using affine equivariant transformed  $L^1$  median with  $\varrho = 5$ . – **Bottom row, left to right:** (i) Filtered using 3D Oja median with  $\varrho = 3$ . – (j) Filtered using 2D Oja median with  $\varrho = 3$ . – (k) Filtered using  $L^1$  median with  $\varrho = 3$ . – (l) Filtered using affine equivariant transformed  $L^1$  median with  $\varrho = 3$ .

### 2.3 Median Filtering of RGB Images

In this section, we consider the filtering of RGB colour image data. The RGB colour space is used here for its simplicity. A comparison with other colour spaces like HSV, HCL, YCbCr etc. is left to future work, and will be important when evaluating the applicability of multivariate median filters in, e.g., denoising applications. It is worth noting, however, that common colour spaces are related via differentiable transforms (with isolated singularities to be observed in some cases). This means that *locally* replacing one colour space with another is just an affine transformation (given by the Jacobian of the colour space transform). For affine equivariant

median filters applied in small neighbourhoods of smooth images, filtering results can therefore be expected to be largely independent of the colour space being used.

Application of the  $L^1$  median to three-channel data is straightforward. Regarding the Oja median filter, it is worth noting that a planar RGB image is a discretisation of a function  $\mathbf{u} : \mathbb{R}^2 \supset \Omega \rightarrow \mathbb{R}^3$ , i.e. a parametrised surface in  $\mathbb{R}^3$ . The values of  $\mathbf{u}$  (RGB triples) within a small patch of  $\Omega$ , such as the structuring element of a pixel, form a surface patch in  $\mathbb{R}^3$ . For a noise-free image, the function  $\mathbf{u}$  can be assumed to be smooth, resulting in almost planar surface patches.

One consequence of this is that the 3D Oja median applied to the RGB triples from a structuring element will be the minimiser of a sum of simplex volumes where virtually all of the simplices are almost degenerated.

On the other hand, the 2D Oja median, which minimises a sum of triangle areas, can easily be applied to these data, which gives us a further option for median filtering of planar RGB images that stands between the  $L^1$  (thus, 1D Oja) and 3D Oja median,

$$\mathbf{m}_{\text{Oja}(2,3)}(\mathcal{X}) := \operatorname{argmin}_{\mathbf{x} \in \mathbb{R}^3} \sum_{1 \leq i < j \leq N} \|[\mathbf{x}, \mathbf{x}_i, \mathbf{x}_j]\|. \quad (7)$$

Of course, the 2D Oja median  $\mathbf{m}_{\text{Oja}(2,3)}$  for general 3D data is not equivariant under affine transformations of  $\mathbb{R}^3$ . However, the 2D Oja median of co-planar data from  $\mathbb{R}^3$  is affine equivariant even with respect to affine transformations of  $\mathbb{R}^3$ . Since the RGB triples being filtered are almost co-planar, it can be expected that a 2D Oja median filter for planar RGB images will display a good approximation to affine equivariance. We include therefore in our experiments four filters based on the standard  $L^1$  median (4), the 2D (7) and 3D (5) Oja median, and the affine equivariant transformed  $L^1$  median (6).

Figure 4 shows results of filtering of an RGB image with these three filters with disc-shaped structuring elements  $D_\varrho$  of different size. (The combination of the full 3D Oja median filter with a structuring element of radius  $\varrho = 10$  is beyond computational possibilities with our simple algorithm and therefore omitted.)

Results indicate that the four median filter variants again give very similar results. As the size of structuring elements increases, the behaviour known from univariate median filters is observed: Small image details are progressively smoothed out, whereas strong edges between homogeneous regions are kept sharp even for larger structuring elements.

Whereas the test image used in Figure 4 contains many fine-scale structures everywhere in the image, we consider in our next experiment, Figure 5, a test image which is dominated by smooth regions, some even with constant colour values, separated by sharp boundaries. This image, shown in Figure 5(a), is almost perfectly noise-free apart from the quantisation noise. Therefore, the RGB triples found within a structuring element are often strictly collinear such that the degeneracy of the Oja median energies becomes an issue in computation. This is demonstrated in Figure 5(b) by the result of (2D) Oja median filtering without regularisation. Note that most edges are substantially blurred. However, at some junctions where values from sufficiently many regions within a small neighbourhood create input data sets of sufficient dimensionality, edges stay sharp. For the further 2D and 3D Oja median filtering in this experiment series, we use therefore the input regularisation as described in Section 2.1, consisting of replacing points with quadruples of simplex corners and subsequent normalisation by principal axis transform. Even with this proceeding, a slight blur remains visible in the Oja results, Figure 5(c), (d) and (g), especially for the larger structuring element (g).

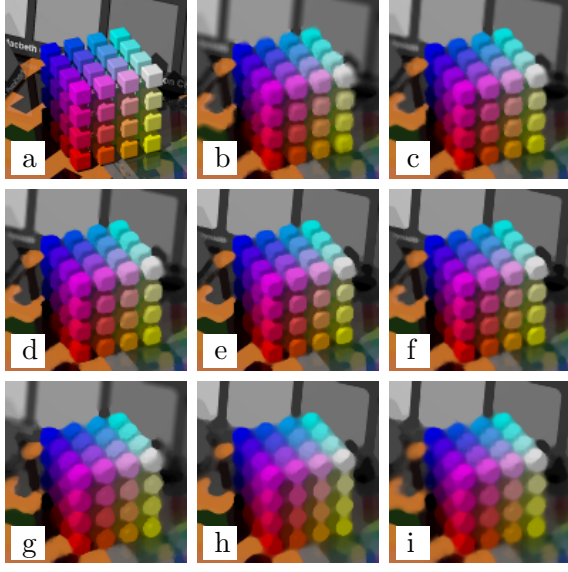


Figure 5: Median filtering of the *Colors* test image using different multivariate medians and disc-shaped structuring elements  $D_\varrho$  of varying radius. The test image is a clipping from the image “Delta E” from <http://brucelindbloom.com/> (©2001–2015 Bruce Justin Lindbloom; research and non-commercial use permitted.) **Top row, left to right:** (a) Original RGB image ( $128 \times 128$  pixels). – (b) Filtered using 2D Oja median with  $\varrho = 3$ , without regularisation. – (c) Filtered using 3D Oja median with  $\varrho = 3$ , with input regularisation. – **Middle row, left to right:** (d) Filtered using 2D Oja median with  $\varrho = 3$ , with input regularisation. – (e) Filtered using  $L^1$  median with  $\varrho = 3$ . – (f) Filtered using affine equivariant transformed  $L^1$  median with  $\varrho = 3$ . – **Bottom row, left to right:** (g) Filtered using 2D Oja median with  $\varrho = 5$ , with input regularisation. – (h) Filtered using  $L^1$  median with  $\varrho = 5$ . – (i) Filtered using affine equivariant transformed  $L^1$  median with  $\varrho = 5$ .

Apart from this, the results of 3D (c) and 2D Oja median filtering (d, g) as well as those of standard (e, h) and affine equivariant transformed  $L^1$  median filtering (f, i) are again largely comparable. They show the structure simplification and rounding of contours known from univariate median filters, whereas edges are kept reasonably sharp.

## 2.4 Geometric Facts about Bivariate $L^1$ and Oja Median

To add some geometric intuition about the  $L^1$  and Oja medians, we consider small point sets in the plane and their medians. The following statements can easily be inferred from standard elementary geometry arguments such as the triangle inequality (for the  $L^1$  median) and multiplicities of covering of the convex hull of input points by the triangles with input and median points as corners (for the 2D Oja median).

In all cases, the  $L^1$  and Oja medians will be located within the convex hull of the input data set (if, in the case of the Oja median, this set is not collinear) due to the convexity of the objective functions being minimised.

1. For two points, the  $L^1$  median criterion is fulfilled equally for all points of their connecting line segment. The Oja median criterion is even fulfilled by all points of the straight line through these points since the Oja median definition degenerates for collinear sets of points.
2. For three points, the  $L^1$  median depends on the sort of triangle they span. If all of its interior angles are smaller than 120 degrees, see Figure 6(a), the sum of distances to the corners is minimised by a unique point known as *Steiner point* or *Fermat-Torricelli point*, from which all sides of the triangle are seen under 120 degree angles. For a triangle with an obtuse corner of at least 120 degrees, this corner is the  $L^1$  median, see Figure 6(b).

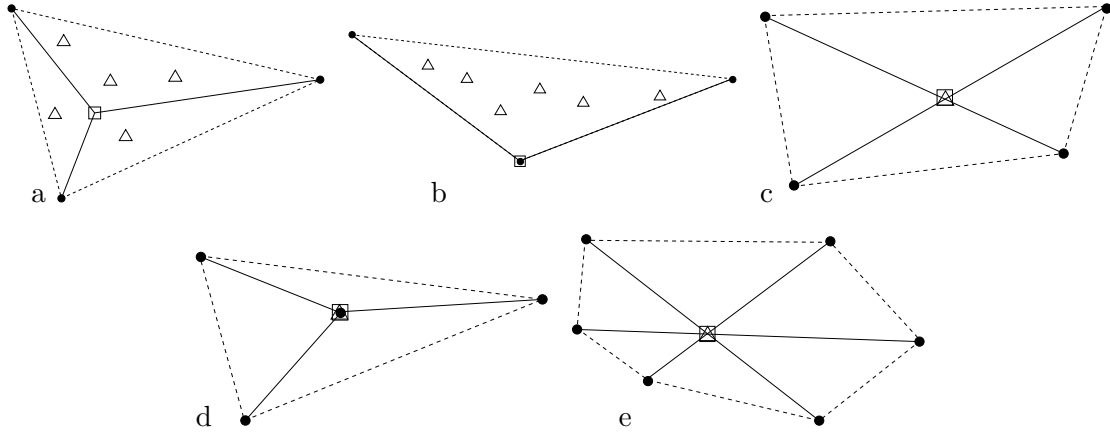


Figure 6: Simple configurations of input data points (solid points) with their  $L^1$  medians (squares) and Oja medians (triangles). **(a)** Three points forming a triangle with all interior angles less than 120 degrees: The  $L^1$  median is the *Steiner point*; any point within the triangle is an Oja median. – **(b)** Three points forming a triangle with an obtuse angle of 120 degrees or more: The obtuse corner is the  $L^1$  median; still, all points within the triangle are Oja medians. – **(c)** Four points forming a convex quadrangle: the  $L^1$  and Oja median coincide at the intersection of the diagonals. – **(d)** Four points whose convex hull is a triangle: the  $L^1$  and Oja median coincide at the data point that is not a corner of the convex hull. – **(e)**  $2n$  points that form a convex  $2n$ -gon (hexagon shown as example) in which all diagonals between opposing points have a common intersection point: its  $L^1$  and Oja median coincide at this intersection point. – From [31].

In contrast, the Oja median criterion is met in both cases by all points of the triangle. This is consistent with the affine equivariance of the Oja median that does not discriminate triangles by shape. Besides, this configuration nicely illustrates how in the Oja median definition simplices take the role of line segments from the univariate median definition: the three-point case of the bivariate Oja median is just the analogue of the two-point case of the univariate median.

3. For four points,  $L^1$  and Oja median always coincide: If the convex hull of the data points is a triangle, then the data point that is not a corner of the convex hull is the median, see Figure 6(d); if it is a convex quadrangle, then the intersection point of its diagonals is the median, see Figure 6(c).
4. The coincidence between  $L^1$  and Oja median continues also in some configurations of more data points. A (non-generic) example is shown in Figure 6(e): A convex  $2n$ -gon in which all the diagonals that bisect the point set (i.e. those that span  $n$  sides) have a common intersection point, features this point as  $L^1$  and Oja median.

We point out two facts that can be learned from these simple configurations. Firstly, bivariate medians, unlike their univariate counterpart, cannot always be chosen from the input data set, but they happen to be input data points in some generic configurations. Only in cases when none of the input points lies sufficiently “in the middle” of the data, a new point is created. Secondly, despite their different definitions, the  $L^1$  and Oja median coincide

in some generic situations, or are not far apart from each other. This adds plausibility to why the image filtering results in Figure 4 and Figure 5 are that similar.

We conclude this section by mentioning a result from [6]: For a non-collinear point set in the plane, there exists always an Oja median (i.e. a point minimising the relevant objective function) that is the intersection of two lines, each of which goes through two data points. Restricting the search for minimisers to the finite set of these intersection points is one of the ingredients in the efficient planar Oja median algorithm from [1].

### 3 Asymptotic Analysis of Multivariate Median Filtering

The reformulation of a local image filter to a space-continuous setting is straightforward. The main modification is that the set of values that results from the selection step and is processed in the aggregation step is now infinite and equipped with a density. This density is induced from the uniform distribution of function arguments in the structuring element in the image domain via the Jacobian of the image function.

As proven in [15], a univariate median filtering step of an image with disc-shaped structuring element of radius  $\varrho$  approximates for  $\varrho \rightarrow 0$  a time step of size  $\tau = \varrho^2/6$  of an explicit scheme for the mean curvature motion PDE. In this section, we will derive PDEs that are approximated in the same sense by multivariate median filters based on  $L^1$  and Oja medians. We will consider images with two or three channels over two- and three-dimensional domains.

Throughout this paper, the structuring element will be a disc  $D_\varrho$  of radius  $\varrho$  for planar images, or a ball  $B_\varrho$  of radius  $\varrho$  for volume images.

#### 3.1 Bivariate Planar Images

We start by considering the case of two-channel images over a planar domain  $\Omega$ , as already studied in [31].

##### 3.1.1 $L^1$ Median

In [31] the result from [33] concerning the  $L^1$  multivariate median filter for images  $\mathbf{u} : \mathbb{R}^2 \supset \Omega \rightarrow \mathbb{R}^n$  was simplified to the bivariate case  $n = 2$ . As the result from [33] needs to be corrected as stated in the Introduction, the statement from [31] is modified as follows.

**Proposition 1** (from [31], corrected). *Let a bivariate image  $\mathbf{u} : \mathbb{R}^2 \supset \Omega \rightarrow \mathbb{R}^2$ ,  $(x, y) \mapsto (u, v)$ , be given. One step of  $L^1$  median filtering with the structuring element  $D_\varrho$  approximates for  $\varrho \rightarrow 0$  an explicit time step of size  $\tau = \varrho^2/6$  of the PDE system*

$$\begin{pmatrix} u_t \\ v_t \end{pmatrix} = \mathbf{S}(\mathbf{D}\mathbf{u}) \begin{pmatrix} u_{\eta\eta} \\ v_{\eta\eta} \end{pmatrix} + \mathbf{T}(\mathbf{D}\mathbf{u}) \begin{pmatrix} u_{\xi\xi} \\ v_{\xi\xi} \end{pmatrix} - 2\mathbf{W}(\mathbf{D}\mathbf{u}) \begin{pmatrix} u_{\xi\eta} \\ v_{\xi\eta} \end{pmatrix} \quad (8)$$

where  $\boldsymbol{\eta}$  is the major, and  $\boldsymbol{\xi}$  the minor eigenvector of the structure tensor  $\mathbf{J} := \mathbf{J}(\mathbf{D}\mathbf{u}) := \nabla u \nabla u^T + \nabla v \nabla v^T = \mathbf{D}\mathbf{u}^T \mathbf{D}\mathbf{u}$ . The coefficient matrices  $\mathbf{S}(\mathbf{D}\mathbf{u})$ ,  $\mathbf{T}(\mathbf{D}\mathbf{u})$  and  $\mathbf{W}(\mathbf{D}\mathbf{u})$  are given by

$$\mathbf{S}(\mathbf{D}\mathbf{u}) := \mathbf{R} \operatorname{diag} \left( Q_1 \left( \frac{|\partial_{\boldsymbol{\eta}} \mathbf{u}|}{|\partial_{\boldsymbol{\xi}} \mathbf{u}|} \right), Q_2 \left( \frac{|\partial_{\boldsymbol{\eta}} \mathbf{u}|}{|\partial_{\boldsymbol{\xi}} \mathbf{u}|} \right) \right) \mathbf{R}^T, \quad (9)$$

$$\mathbf{T}(\mathbf{D}\mathbf{u}) := \mathbf{R} \operatorname{diag} \left( Q_2 \left( \frac{|\partial_{\boldsymbol{\xi}} \mathbf{u}|}{|\partial_{\boldsymbol{\eta}} \mathbf{u}|} \right), Q_1 \left( \frac{|\partial_{\boldsymbol{\xi}} \mathbf{u}|}{|\partial_{\boldsymbol{\eta}} \mathbf{u}|} \right) \right) \mathbf{R}^T, \quad (10)$$

$$\mathbf{W}(\mathbf{D}\mathbf{u}) := \mathbf{R} \begin{pmatrix} 0 & \frac{|\partial_{\boldsymbol{\eta}}\mathbf{u}|}{|\partial_{\boldsymbol{\xi}}\mathbf{u}|} Q_1\left(\frac{|\partial_{\boldsymbol{\eta}}\mathbf{u}|}{|\partial_{\boldsymbol{\xi}}\mathbf{u}|}\right) \\ \frac{|\partial_{\boldsymbol{\xi}}\mathbf{u}|}{|\partial_{\boldsymbol{\eta}}\mathbf{u}|} Q_1\left(\frac{|\partial_{\boldsymbol{\xi}}\mathbf{u}|}{|\partial_{\boldsymbol{\eta}}\mathbf{u}|}\right) & 0 \end{pmatrix} \mathbf{R}^T, \quad (11)$$

where  $\mathbf{R} = (\mathbf{D}\mathbf{u}^{-1})^T \mathbf{P} \text{diag}(|\partial_{\boldsymbol{\eta}}\mathbf{u}|, |\partial_{\boldsymbol{\xi}}\mathbf{u}|)$  is a rotation matrix that depends on the Jacobian  $\mathbf{D}\mathbf{u}$  of  $\mathbf{u}$  and the eigenvector matrix  $\mathbf{P} = (\boldsymbol{\eta} \mid \boldsymbol{\xi})$  of  $\mathbf{J}$ . The functions  $Q_1, Q_2 : [0, \infty] \rightarrow \mathbb{R}$  are given by the quotients of elliptic integrals

$$Q_1(\lambda) = \frac{3 \iint_{D_1(\mathbf{0})} s^2 t^2 / (s^2 + \lambda^2 t^2)^{3/2} \, ds \, dt}{\iint_{D_1(\mathbf{0})} s^2 / (s^2 + \lambda^2 t^2)^{3/2} \, ds \, dt}, \quad (12)$$

$$Q_2(\lambda) = \frac{3 \iint_{D_1(\mathbf{0})} t^4 / (s^2 + \lambda^2 t^2)^{3/2} \, ds \, dt}{\iint_{D_1(\mathbf{0})} t^2 / (s^2 + \lambda^2 t^2)^{3/2} \, ds \, dt} \quad (13)$$

for  $\lambda \in (0, \infty)$ , together with the limits  $Q_1(0) = Q_2(0) = 1$ ,  $Q_1(\infty) = Q_2(\infty) = 0$ .

*Remark 1.* The vectors  $\boldsymbol{\eta}$  and  $\boldsymbol{\xi}$  used in (8)–(11) are the directions of greatest and least change of the bivariate function  $\mathbf{u}$ , thus the closest analoga to gradient and level line directions of univariate images, see [12]. The use of these image-adaptive local coordinates characterises (8) as a curvature-based PDE remotely similar to the (mean) curvature motion PDE approximated by univariate median filtering.

The proof of the proposition relies on the following statement which is corrected from [33].

**Lemma 1** (from [33], corrected). *Let  $\mathbf{u}$  be given as in Proposition 1, and the origin  $\mathbf{0} = (0, 0)$  be an inner point of  $\Omega$ . Assume that the Jacobian  $\mathbf{D}\mathbf{u}(\mathbf{0})$  is diagonal, i.e.  $u_y = v_x = 0$ , and  $u_x \geq v_y > 0$ . Then one step of  $L^1$  median filtering with the structuring element  $D_\varrho$  at  $\mathbf{0}$  approximates for  $\varrho \rightarrow 0$  an explicit time step of size  $\tau = \varrho^2/6$  of the PDE system*

$$u_t = Q_1\left(\frac{u_x}{v_y}\right) u_{xx} + Q_2\left(\frac{v_y}{u_x}\right) u_{yy} - \frac{2u_x}{v_y} Q_1\left(\frac{u_x}{v_y}\right) v_{xy}, \quad (14)$$

$$v_t = Q_2\left(\frac{u_x}{v_y}\right) v_{xx} + Q_1\left(\frac{v_y}{u_x}\right) v_{yy} - \frac{2v_y}{u_x} Q_1\left(\frac{v_y}{u_x}\right) u_{xy}, \quad (15)$$

with the coefficient functions  $Q_1, Q_2$  as stated in Proposition 1.

*Remark 2.* The elliptic integrals in the coefficient expressions  $Q_1(\lambda)$  and  $Q_2(\lambda)$  can in general not be evaluated in closed form. However, they are connected by

$$Q_2(\lambda) = 1 - Q_1(\lambda^{-1}). \quad (16)$$

*Remark 3.* In the case  $u_x = 1, v_y = 1$ , the coefficients of (14), (15) simplify via  $Q_1(1) = 1/4$ ,  $Q_2(1) = 3/4$  such that one obtains

$$u_t = \frac{1}{4} u_{xx} + \frac{3}{4} u_{yy} - \frac{1}{2} v_{xy}, \quad (17)$$

$$v_t = \frac{3}{4} v_{xx} + \frac{1}{4} v_{yy} - \frac{1}{2} u_{xy}. \quad (18)$$

*Remark 4.* Note that for  $\lambda \rightarrow \infty$ ,  $\lambda Q_1(\lambda)$  goes to zero such that the coefficients for  $v_{xy}$  in (14) and for  $u_{xy}$  in (15) are globally bounded for arbitrary  $u_x, v_y$ , and in the limit case  $v_y = 0$  one has the decoupled PDEs  $u_t = u_{yy}, v_t = v_{xx}$ .

*Remark 5.* Univariate median filtering is contained in the statement of Lemma 1 when  $v_y$  is sent to 0. In this case, the first PDE (14) becomes  $u_t = u_{yy}$  by virtue of  $Q_1(\infty) = 0$ ,  $Q_2(0) = 1$ , and the previous remark. This translates to  $u_t = u_{\xi\xi}$  in the general setting of Proposition 1, i.e. the (mean) curvature motion equation, thus reproducing exactly the result of [15].

*Proof of Proposition 1.* Consider an arbitrary fixed location  $(x^*, y^*)$ . By applying rotations with  $\mathbf{P}$  in the  $x$ - $y$  plane and with  $\mathbf{R}$  in the  $u$ - $v$  plane,  $x, y$  can be aligned with the (orthogonal) major and minor eigenvector directions  $\boldsymbol{\eta}$  and  $\boldsymbol{\xi}$  of the structure tensor  $\mathbf{J}(\nabla u, \nabla v)$  at  $(x^*, y^*)$ , and  $u, v$  with the corresponding derivatives  $\partial_{\boldsymbol{\eta}} \mathbf{u}$ ,  $\partial_{\boldsymbol{\xi}} \mathbf{u}$ . Then Lemma 1 can be applied. Reverting the rotations in the  $x$ - $y$  and  $u$ - $v$  planes, the PDE system (14)–(15) turns into the system (8)–(11) of the proposition.  $\square$

*Remark 6.* Equivariance of the PDE (8) with regard to Euclidean transformations of the  $u$ - $v$  plane follows immediately from its derivation for a special case and transfer to the general case by a Euclidean transformation.

### 3.1.2 Oja Median

Next we turn to the Oja median, which in the bivariate case under consideration is defined as the minimiser of the total area of triangles each formed by two given data points and the median point. The following result was proven in [31].

**Theorem 1** (from [31]). *Let a bivariate image  $\mathbf{u} : \mathbb{R}^2 \supset \Omega \rightarrow \mathbb{R}^2$ ,  $(x, y) \mapsto (u, v)$ , be given. At any location where  $\det \mathbf{D}\mathbf{u} \neq 0$ , one step of Oja median filtering of  $\mathbf{u}$  with the structuring element  $D_\varrho$  approximates for  $\varrho \rightarrow 0$  an explicit time step of size  $\tau = \varrho^2/24$  of the PDE system*

$$\begin{pmatrix} u_t \\ v_t \end{pmatrix} = 2 \begin{pmatrix} u_{xx} + u_{yy} \\ v_{xx} + v_{yy} \end{pmatrix} - \mathbf{A}(\mathbf{D}\mathbf{u}) \begin{pmatrix} u_{xx} - u_{yy} \\ v_{yy} - v_{xx} \end{pmatrix} - \mathbf{B}(\mathbf{D}\mathbf{u}) \begin{pmatrix} u_{xy} \\ v_{xy} \end{pmatrix} \quad (19)$$

with the coefficient matrices

$$\mathbf{A}(\mathbf{D}\mathbf{u}) := \frac{1}{u_x v_y - u_y v_x} \begin{pmatrix} u_x v_y + u_y v_x & 2u_x u_y \\ 2v_x v_y & u_x v_y + u_y v_x \end{pmatrix}, \quad (20)$$

$$\mathbf{B}(\mathbf{D}\mathbf{u}) := \frac{2}{u_x v_y - u_y v_x} \begin{pmatrix} -u_x v_x + u_y v_y & u_x^2 - u_y^2 \\ -v_x^2 + v_y^2 & u_x v_x - u_y v_y \end{pmatrix}. \quad (21)$$

The proof of this theorem relies on the following lemma.

**Lemma 2** (from [31]). *Let  $\mathbf{u}$  be given as in Theorem 1, and  $\mathbf{0} = (0, 0)$  be an inner point of  $\Omega$ . Assume that  $\mathbf{D}\mathbf{u}(\mathbf{0})$  is the  $2 \times 2$  unit matrix  $\mathbf{I}$ . At  $\mathbf{x} = \mathbf{0}$ , one step of Oja median filtering of  $\mathbf{u}$  with the structuring element  $D_\varrho$  then approximates for  $\varrho \rightarrow 0$  an explicit time step of size  $\tau = \varrho^2/24$  of the PDE system*

$$u_t = u_{xx} + 3u_{yy} - 2v_{xy}, \quad (22)$$

$$v_t = 3v_{xx} + v_{yy} - 2u_{xy}. \quad (23)$$

*Remark 7.* Note that the PDE system (22), (23) coincides exactly with (17), (18), the  $L^1$  result for the same case  $\mathbf{D}\mathbf{u}(\mathbf{0}) = \mathbf{I}$ , except for a rescaling of the time  $t$  by a factor 4 in compensation for the different time step size  $\varrho^2/24$  in Lemma 2 opposed to  $\varrho^2/6$  in Lemma 1.

This lemma is proven in the appendix in two slightly different ways. The first proof, in Appendix A, goes back to [31] and is presented here in slightly more detail. The new proof in Appendix B is more straightforward. The reason why the first proof is also kept in this paper is that it is the blueprint for subsequent proofs in this paper, whereas the approach of the second proof would be more cumbersome to extend to these cases.

Both proofs start from a Taylor expansion of  $(u, v)^T$  within the structuring element, and express the gradient of the objective function minimised by the Oja median in terms of the Taylor coefficients. The median value is found as the point in the  $u$ - $v$  plane for which this gradient vanishes. In both cases, the gradient itself is linearised w.r.t. the Taylor coefficients.

In the first proof, Appendix A, the calculation of the gradient is organised by integration over directions in the  $u$ - $v$  plane, and the influences of the individual Taylor coefficients are estimated separately by integrals over the respective deformed structuring elements.

In contrast, the second proof in Appendix B calculates the gradient by integration in the  $x$ - $y$  plane. The main idea here is to find for each point  $(x_1, y_1)$  a splitting of the structuring element into two regions: one region contains all points  $(x_2, y_2)$  for which the median candidate point and the images of  $(x_1, y_1)$  and  $(x_2, y_2)$  form in this order a positively oriented triangle in the  $u$ - $v$  plane whereas for  $(x_2, y_2)$  in the other region this triangle has negative orientation. This approach allows to calculate the entire gradient with its dependencies on all Taylor coefficients at once.

*Proof of Theorem 1.* To prove the Theorem, we consider the median of the values  $\mathbf{u}(x, y)$  within the Euclidean  $\varrho$ -neighbourhood of  $(0, 0)$ , and assume that the Jacobian  $\mathbf{D} := D\mathbf{u}(\mathbf{0})$  is regular as requested by the hypothesis of the Theorem.

We transform the  $u$ - $v$  plane to variables  $\hat{\mathbf{u}}$  via

$$\hat{\mathbf{u}} = \mathbf{D}^{-1} \mathbf{u} . \quad (24)$$

The affine equivariance of Oja's simplex median ensures that also the median  $\mathbf{u}^*$  of the values  $\mathbf{u}$  within the structuring element follows this transform. The transformed data  $\hat{\mathbf{u}}$  satisfy the hypothesis  $D\hat{\mathbf{u}}(\mathbf{0}) = \mathbf{I}$  of Lemma 2, thus the median filtering step for these values approximates the PDE system (22), (23).

We transfer the result to the general situation of the theorem by the inverse transform of (24). Rewriting (22), (23) as

$$\begin{aligned} \hat{\mathbf{u}}_t &= \begin{pmatrix} \hat{u}_{xx} + 3\hat{u}_{yy} - 2\hat{v}_{xy} \\ 3\hat{v}_{xx} + \hat{v}_{yy} - 2\hat{u}_{xy} \end{pmatrix} \\ &= 2(\hat{\mathbf{u}}_{xx} + \hat{\mathbf{u}}_{yy}) + \begin{pmatrix} 1 & 0 \\ 0 & -1 \end{pmatrix} (\hat{\mathbf{u}}_{yy} - \hat{\mathbf{u}}_{xx}) - 2 \begin{pmatrix} 0 & 1 \\ 1 & 0 \end{pmatrix} \hat{\mathbf{u}}_{xy} \\ &= 2 \mathbf{D}^{-1}(\mathbf{u}_{xx} + \mathbf{u}_{yy}) + \begin{pmatrix} 1 & 0 \\ 0 & -1 \end{pmatrix} \mathbf{D}^{-1}(\mathbf{u}_{yy} - \mathbf{u}_{xx}) - 2 \begin{pmatrix} 0 & 1 \\ 1 & 0 \end{pmatrix} \mathbf{D}^{-1} \mathbf{u}_{xy} \end{aligned} \quad (25)$$

we obtain

$$\mathbf{u}_t = 2 \mathbf{D} \mathbf{D}^{-1}(\mathbf{u}_{xx} + \mathbf{u}_{yy}) + \mathbf{D} \begin{pmatrix} 1 & 0 \\ 0 & -1 \end{pmatrix} \mathbf{D}^{-1}(\mathbf{u}_{yy} - \mathbf{u}_{xx}) - 2 \mathbf{D} \begin{pmatrix} 0 & 1 \\ 1 & 0 \end{pmatrix} \mathbf{D}^{-1} \mathbf{u}_{xy} \quad (26)$$

which expands to the PDE system (19) with coefficient matrices (20), (21) as stated in the theorem.  $\square$

*Remark 8.* The derivation of the PDE of Theorem 1 by affine transformation immediately implies its affine equivariance. The final PDE itself is even equivariant under affine transformations of the  $x$ - $y$  plane. Regarding the approximation of Oja median filtering, however, the Euclidean disc-shaped structuring element allows only for Euclidean transformations of the  $x$ - $y$  plane.

### 3.1.3 Interpretation of Bivariate Median Filter PDEs

The geometric meaning of the PDE systems from Sections 3.1.1 and 3.1.2 is best discussed by considering the principal components of the local variation of the data. In the general setting of Proposition 1 and Theorem 1 the channelwise evolutions  $u_t$ ,  $v_t$  are mixtures of these principal components, which obscures their geometric significance. In the case of diagonal Jacobian  $D\mathbf{u}$  as in the hypothesis of Lemma 1 the channels are decorrelated and represent these principal components.

We base our discussion therefore on the PDE system (14), (15) from Lemma 1 for the  $L^1$  median, and

$$u_t = u_{xx} + 3u_{yy} - 2u_x v_{xy}/v_y, \quad (27)$$

$$v_t = 3v_{xx} + v_{yy} - 2v_y u_{xy}/u_x \quad (28)$$

for the Oja median which is the straightforward adaptation of the PDE system (22), (23) from Lemma 2 to the situation of a general diagonal Jacobian.

Comparing the two PDE systems, we see that in each of them an isotropic linear diffusion contribution  $(u_{xx} + u_{yy}, v_{xx} + v_{yy})^T$  is combined with an additional directional diffusion  $(u_{yy}, v_{xx})^T$  and a cross-effect contribution  $(u_x v_{xy}/v_y, v_y u_{xy}/u_x)^T$  with some weights.

For the directional diffusion term it is worth noticing that the  $y$  direction for  $u$ , and  $x$  direction for  $v$  are the level-line directions of the individual components, i.e. this term represents independent (mean) curvature motion evolutions for the two principal components.

The mixed second derivatives of the third term express the torsion of the graphs of the two principal components, and are multiplied with scaling factors that adapt between the componentwise gradients  $u_x$  and  $v_y$ .

In the Oja median PDE, the weights of these terms are constant. The first two terms act independent in the two components such that the torsion-based cross-effect term constitutes the only coupling between principal components.

In contrast, the coefficient functions  $Q_1$  and  $Q_2$  in the  $L^1$  case modulate also the diffusion and curvature terms and create additional cross-effects between the principal components. This is due to the more rigid Euclidean structure underlying the  $L^1$  median definition, and also makes it sensible to write the PDE for the general case using the eigenvector directions  $\boldsymbol{\eta}$  and  $\boldsymbol{\xi}$  of the structure tensor as done in Proposition 1. In the decoupled setting of Theorem 1 these directions have no meaning. This is plausible because these eigenvectors are strongly related with a Euclidean geometry concept of the  $u$ - $v$  plane, and are thereby inappropriate for an affine equivariant process like Oja median filtering.

In detail, the effect of the coefficient functions  $Q_1$  and  $Q_2$  is steered by the relative weight of the principal components, namely  $u_x$  and  $v_y$  in the aligned case under consideration. Denoting the principal component with stronger gradient as dominant component, and the other as non-dominant component, one sees that the more pronounced the dominance of the first principal component is, the more does it steer the evolution also of the other principal

component (as the joint pseudo-gradient vector  $\boldsymbol{\eta}$  aligns more and more with the gradient vector of the dominant component).

### 3.1.4 Discussion of the Degenerate Case $\det \mathbf{D}\mathbf{u} = 0$

The right-hand side of equation (19) is undefined at locations where  $\det \mathbf{D}\mathbf{u} = 0$ . While the weights for the second derivatives  $\mathbf{u}_{xx}$  and  $\mathbf{u}_{yy}$  remain bounded when  $\det \mathbf{D}\mathbf{u}$  goes to zero, the weights of the mixed terms  $u_{xy}$  and  $v_{xy}$  can take arbitrarily large values in this case. To see more precisely what is going on, let us consider once more the case of a diagonal Jacobian  $\mathbf{D}\mathbf{u}$ , and keep  $u_x = 1$  fixed while  $v_y$  goes to zero. Then the weight of  $v_{xy}$  in the PDE (22) for  $u_t$  goes to infinity with  $1/v_y$  whereas the weight of  $u_{xy}$  in the PDE (23) for  $v_t$  goes to zero. This is different from the situation for the  $L^1$  median where the coefficients of the mixed terms  $u_{xy}$  and  $v_{xy}$  were bounded for all values of the gradient. However, it is easy to see that for an affine equivariant median there is basically no way out: As soon as there is a non-zero influence of  $v_{xy}$  on  $u_t$ , it must scale in this way by affine equivariance.

Keeping in mind, however, that  $u_x$  and  $v_y$  for diagonal  $\mathbf{D}\mathbf{u}$  are the channelwise gradient directions, it becomes evident that divergent behaviour, such as  $v_y$  going to zero while  $u_x v_{xy}$  in the numerator is nonzero, can affect only isolated points in the plane, and can thereby be cured by using the concept of viscosity solutions. Vanishing of  $v_y$  in an extended region is only possible if the function  $v$  is constant in this region such that also  $v_{xy}$  vanishes, allowing to fill this definition gap in the term  $u_x v_{xy}/v_y$  with zero.

This is also in harmony with the behaviour of the median filter itself. As the median of a set of data values is restricted to the convex hull of the input data, infinite amplification of variations from the  $v$  to the  $u$  component and vice versa is impossible. As the PDE is only approximated in the limit  $\varrho \rightarrow 0$ , it can moreover be expected that for positive  $\varrho$ , the sensitivity of the  $u$  component of the median filtering result to  $v_{xy}$  will be dampened nonlinearly which would be reflected in higher order terms neglected in the PDE derivation.

Structuring elements with varying radius  $\varrho$  can be translated to fixed radius by scaling the second-order Taylor coefficients of the bivariate function, i.e.  $u_{xx}(\mathbf{0})$ , etc., with  $\varrho$ . Deviations from the PDE behaviour for positive  $\varrho$  can therefore be studied equivalently by investigating nonlinearities in the response of the median to increasing values of the derivatives  $u_{xx}$  within a fixed structuring element. In Section 4.1.3 we will demonstrate this dampening by a numerical experiment.

### 3.1.5 Affine Equivariant Transformed $L^1$ Median

As pointed out in Remark 7, the PDEs approximated by the bivariate  $L^1$  and Oja median filters coincide when the Jacobian of the image being filtered is the unit matrix. The difference between the  $L^1$  case in Proposition 1 and the Oja case in Theorem 1 is that the affine equivariance of the latter allows to derive the general case by affine transformations from the special case  $\mathbf{D}\mathbf{u} = \mathbf{I}$ , whereas the  $L^1$  median admits only Euclidean transformations such that its general case needs to be derived from the wider setting of Lemma 1 where  $\mathbf{D}\mathbf{u}$  can be arbitrary diagonal. This is where the complicated coefficient functions of Proposition 1 have their origin.

On the other hand, one can combine the minimisation principle of the  $L^1$  median with the affine transformation concept from the proof of Theorem 1 to design a bivariate space-continuous image filter as follows.

**Definition 1** (Space-continuous affine equivariant transformed  $L^1$  median filter.). Let a function  $\mathbf{u} : \mathbb{R}^2 \supset \Omega \rightarrow \mathbb{R}^2$  and the structuring element  $D_\varrho$  be given. For each location  $\mathbf{x}_0 \in \Omega$  with  $\det D\mathbf{u}(\mathbf{x}_0) \neq 0$ , transform the function values  $\mathbf{u}(\mathbf{x})$  for  $\mathbf{x} \in \mathbf{x}_0 + D_\varrho$  via  $\hat{\mathbf{u}} = D\mathbf{u}(\mathbf{x}_0)^{-1}\mathbf{u}$ . Determine the  $L^1$  median  $\hat{\mathbf{u}}^*$  of the data  $\hat{\mathbf{u}}$ . Transform  $\hat{\mathbf{u}}^*$  back to  $\mathbf{u}^*(\mathbf{x}_0) = D\mathbf{u}(\mathbf{x}_0)\hat{\mathbf{u}}^*$ . The image filter that transfers the input function  $\mathbf{u} : \Omega \rightarrow \mathbb{R}^2$  to the function  $\mathbf{u}^* : \Omega \rightarrow \mathbb{R}^2$  is called affine equivariant transformed  $L^1$  median filter.

Affine equivariance of this image filter is clear by construction. By inheritance from the underlying  $L^1$  median it approximates in the case  $D\mathbf{u} = \mathbf{I}$  the same PDEs for  $\varrho \rightarrow 0$  as the  $L^1$  and Oja median filters. Due to its construction from this special case via the affine transform with  $D\mathbf{u}$  it finally approximates in the general (non-degenerate) situation the same PDEs as the Oja median filter. We have thus the following corollary.

**Corollary 1.** *Let a bivariate image  $\mathbf{u} : \mathbb{R}^2 \supset \Omega \rightarrow \mathbb{R}^2$ ,  $(x, y) \mapsto (u, v)$ , be given. At any location where  $\det D\mathbf{u} \neq 0$ , one step of affine equivariant transformed  $L^1$  median filtering of  $\mathbf{u}$  with the structuring element  $D_\varrho$  approximates for  $\varrho \rightarrow 0$  an explicit time step of size  $\tau = \varrho^2/24$  of the PDE system (19) from Theorem 1.*

Using this approach for practical, i.e. discrete image filtering, requires to estimate from the discrete image data within a structuring element the Jacobian  $D\mathbf{u}$ . But the space-continuous data within  $\mathbf{x}_0 + D_\varrho$  represent a distribution whose covariance matrix asymptotically approaches  $D\mathbf{u}$  as  $\varrho \rightarrow 0$ . Thus, estimation of this covariance matrix from sampled data as used in the transformation–retransformation  $L^1$  median approaches [10, 17, 22] and as used in our experimental demonstration in Section 2.3 is exactly what is needed here. Hence, the filter from Definition 1 is a space-continuous version of the discrete transformation–retransformation  $L^1$  median filter.

Corollary 1 therefore states that as bivariate image filters, *the affine equivariant transformed  $L^1$  median is asymptotically equivalent to the Oja median*. Further analysis in this section as well as numerical evidence in Section 4.1 will reveal that this asymptotic equivalence generalises beyond the bivariate case.

## 3.2 Three-Channel Volume Images

As the next step in our theoretical investigation, we increase the dimensions of image and value domain equally to three, thus arriving at three-channel volume images. A possible application would be given by 3D deformation fields as they arise in elastic registration of medical 3D data sets. We do, however, not aim at applications of this setting within this work, and include it primarily for the theoretical completeness. Our focus in this context will be on affine equivariant median filters.

### 3.2.1 Oja Median

The first three-channel volume filter we consider will be based on the 3D Oja median in the sense of (5) minimising a sum of volumes of tetrahedra.

**Theorem 2.** *Let a three-channel volume image  $\mathbf{u} : \mathbb{R}^3 \supset \Omega \rightarrow \mathbb{R}^3$ ,  $(x, y, z) \mapsto (u, v, w)$ , be given. At any location where  $\det D\mathbf{u} \neq 0$ , one step of Oja median filtering of  $\mathbf{u}$  with the structuring element  $B_\varrho$  approximates for  $\varrho \rightarrow 0$  an explicit time step of size  $\tau = \varrho^2/60$  of the*

PDE system

$$\begin{pmatrix} u_t \\ v_t \\ w_t \end{pmatrix} = 5 \begin{pmatrix} u_{xx} + u_{yy} + u_{zz} \\ v_{xx} + v_{yy} + v_{zz} \\ w_{xx} + w_{yy} + w_{zz} \end{pmatrix} + \mathbf{A}_1(\mathbf{D}\mathbf{u}) \begin{pmatrix} u_{yy} - u_{xx} \\ v_{yy} - v_{xx} \\ w_{yy} - w_{xx} \end{pmatrix} + \mathbf{A}_2(\mathbf{D}\mathbf{u}) \begin{pmatrix} u_{zz} - u_{xx} \\ v_{zz} - v_{xx} \\ w_{zz} - w_{xx} \end{pmatrix} \\ - 3 \mathbf{B}_1(\mathbf{D}\mathbf{u}) \begin{pmatrix} u_{xy} \\ v_{xy} \\ w_{xy} \end{pmatrix} - 3 \mathbf{B}_2(\mathbf{D}\mathbf{u}) \begin{pmatrix} u_{xz} \\ v_{xz} \\ w_{xz} \end{pmatrix} - 3 \mathbf{B}_3(\mathbf{D}\mathbf{u}) \begin{pmatrix} u_{yz} \\ v_{yz} \\ w_{yz} \end{pmatrix} \quad (29)$$

where for  $\mathbf{D} := \mathbf{D}\mathbf{u}$  the coefficient matrices are given by

$$\mathbf{A}_1(\mathbf{D}) := \mathbf{I} - 3 \mathbf{D} \text{diag}(0, 1, 0) \mathbf{D}^{-1}, \quad (30)$$

$$\mathbf{A}_2(\mathbf{D}) := \mathbf{I} - 3 \mathbf{D} \text{diag}(0, 0, 1) \mathbf{D}^{-1}, \quad (31)$$

$$\mathbf{B}_1(\mathbf{D}) := \mathbf{D} \begin{pmatrix} 0 & 1 & 0 \\ 1 & 0 & 0 \\ 0 & 0 & 0 \end{pmatrix} \mathbf{D}^{-1}, \quad (32)$$

$$\mathbf{B}_2(\mathbf{D}) := \mathbf{D} \begin{pmatrix} 0 & 0 & 1 \\ 0 & 0 & 0 \\ 1 & 0 & 0 \end{pmatrix} \mathbf{D}^{-1}, \quad (33)$$

$$\mathbf{B}_3(\mathbf{D}) := \mathbf{D} \begin{pmatrix} 0 & 0 & 0 \\ 0 & 0 & 1 \\ 0 & 1 & 0 \end{pmatrix} \mathbf{D}^{-1}. \quad (34)$$

The proof of this theorem proceeds analogously to the proof of Theorem 1, with the use of the following lemma that is analogous to Lemma 2.

**Lemma 3.** *Let  $\mathbf{u}$  be given as in Theorem 2, with  $\mathbf{0} = (0, 0, 0)$  being in the interior of  $\Omega$ . Assume that  $\mathbf{D}\mathbf{u}(\mathbf{0})$  is the  $3 \times 3$  unit matrix  $\mathbf{I}$ . At  $\mathbf{x} = \mathbf{0}$ , one step of Oja median filtering of  $\mathbf{u}$  with the structuring element  $B_\varrho$  then approximates for  $\varrho \rightarrow 0$  an explicit time step of size  $\tau = \varrho^2/20$  of the PDE system*

$$u_t = u_{xx} + 2(u_{yy} + u_{zz}) - (v_{xy} + w_{xz}) \quad (35)$$

$$v_t = v_{yy} + 2(v_{xx} + v_{zz}) - (u_{xy} + w_{yz}) \quad (36)$$

$$w_t = w_{zz} + 2(w_{xx} + w_{yy}) - (u_{xz} + v_{yz}). \quad (37)$$

The proof of this lemma extends the first proof of Lemma 2 and is given in Appendix C.

*Remark 9.* In full analogy with the bivariate case, see Section 3.1.3, the PDE system can be interpreted in terms of the principal components of local data variation, which appear decorrelated in Lemma 3. Again, the PDEs combine isotropic diffusion with componentwise mean curvature motion given by  $(u_{yy} + u_{zz}, v_{xx} + v_{zz}, w_{xx} + w_{zz})^T$  and cross-effect terms. The latter couple each pair of principal components by mutual influence based on the torsion of these components in the plane spanned by both.

### 3.2.2 Affine Equivariant Transformed $L^1$ Median

Definition 1 can be applied verbatim to define an affine equivariant transformed  $L^1$  median filter for functions  $\mathbf{u} : \mathbb{R}^3 \supset \Omega \rightarrow \mathbb{R}^3$ , which we will consider now.

**Proposition 2.** *Let a three-channel volume image  $\mathbf{u} : \mathbb{R}^3 \supset \Omega \rightarrow \mathbb{R}^3$ ,  $(x, y, z) \mapsto (u, v, w)$ , be given. At any location where  $\det \mathbf{D}\mathbf{u} \neq 0$ , one step of affine equivariant transformed  $L^1$  median filtering of  $\mathbf{u}$  with the structuring element  $B_\varrho$  approximates for  $\varrho \rightarrow 0$  an explicit time step of size  $\tau = \varrho^2/60$  of the PDE system (29) with the coefficient matrices (30)–(34) as stated in Theorem 2.*

This proposition is a consequence of the following lemma.

**Lemma 4.** *Let  $\mathbf{u}$  be given as in Proposition 2. Assume that  $\mathbf{D}\mathbf{u}(\mathbf{0})$  is the  $3 \times 3$  unit matrix  $\mathbf{I}$ . At  $\mathbf{x} = \mathbf{0}$ , one step of  $L^1$  median filtering of  $\mathbf{u}$  with the structuring element  $B_\varrho$  then approximates for  $\varrho \rightarrow 0$  an explicit time step of size  $\tau = \varrho^2/20$  of the PDE system (35)–(37) from Lemma 3.*

The proof of this lemma is based on the same principle as the proof of Lemma 1 in [33], extended from two to three dimensions but at the same time simplified by restricting the Jacobian  $\mathbf{D}\mathbf{u}$  to the unit matrix. It is detailed in Appendix D.

We remark that there is no serious technical obstacle to generalising this proof even to arbitrary diagonal Jacobians, which would yield a PDE approximation result for the standard  $L^1$  median in three dimensions. As in Proposition 1, quotients of elliptic integrals would appear as coefficient functions. With our focus on affine equivariant filters, we do not need this generality here.

### 3.3 Three-Channel Planar Images

So far we have considered settings in which the number of dimensions of the image domain  $\Omega$  equalled that of the data space. There are, however, important classes of image data for which this is not the case, with RGB colour images over planar domains being the most prominent example. As our last dimensional setting, we will therefore consider three-channel images over planar domains. The Jacobian of such an image is a  $3 \times 2$  matrix field. The generic case is therefore no longer given by an invertible Jacobian but just by the rank of the Jacobian being maximal (2), which requires adjusting several arguments. Our focus will again be on affine equivariant filters.

#### 3.3.1 2D Oja Median

With regard to the degeneracy of the 3D Oja median in the sense of (5) in the case of three-channel data over a planar domain that has already been discussed in Section 2.3 we choose the 2D Oja median in the sense of (7) for our theoretical analysis.

**Theorem 3.** *Let a three-channel planar image  $\mathbf{u} : \mathbb{R}^2 \supset \Omega \rightarrow \mathbb{R}^3$ ,  $(x, y) \mapsto (u, v, w)$ , be given. At any location where the  $3 \times 2$  matrix  $\mathbf{D}\mathbf{u}$  has rank 2, one step of 2D Oja median filtering of  $\mathbf{u}$  with the structuring element  $D_\varrho$  approximates for  $\varrho \rightarrow 0$  an explicit time step of size  $\tau = \varrho^2/24$  of the PDE system*

$$\begin{pmatrix} u_t \\ v_t \\ w_t \end{pmatrix} = 2 \begin{pmatrix} u_{xx} + u_{yy} \\ v_{xx} + v_{yy} \\ w_{xx} + w_{yy} \end{pmatrix} + \mathbf{A}(\mathbf{D}\mathbf{u}) \begin{pmatrix} u_{yy} - u_{xx} \\ v_{yy} - v_{xx} \\ w_{yy} - w_{xx} \end{pmatrix} - 2 \mathbf{B}(\mathbf{D}\mathbf{u}) \begin{pmatrix} u_{xy} \\ v_{xy} \\ w_{xy} \end{pmatrix} \quad (38)$$

where for  $\mathbf{D} := \mathbf{D}\mathbf{u} = (\partial_x \mathbf{u} \mid \partial_y \mathbf{u})$  and

$$\mathbf{D}_3 := \left( \partial_x \mathbf{u} \mid \partial_y \mathbf{u} \mid \partial_x \mathbf{u} \times \partial_y \mathbf{u} \right) \quad (39)$$

the coefficient matrices are given by

$$\mathbf{A}(\mathbf{D}) := \mathbf{D}_3 \operatorname{diag}(1, -1, 0) \mathbf{D}_3^{-1}, \quad (40)$$

$$\mathbf{B}(\mathbf{D}) := \mathbf{D}_3 \begin{pmatrix} 0 & 1 & 0 \\ 1 & 0 & 0 \\ 0 & 0 & 0 \end{pmatrix} \mathbf{D}_3^{-1}. \quad (41)$$

*Remark 10.* Note that  $\mathbf{D}_3$ , the  $3 \times 3$  matrix obtained by enlarging the  $2 \times 3$  Jacobian  $\mathbf{D}\mathbf{u}$  with a third column orthogonal to the first two ones, is regular if and only if  $\mathbf{D}\mathbf{u}$  has rank 2 as required in the hypothesis of the theorem. The transformed variables  $\hat{\mathbf{u}} := \mathbf{D}_3^{-1}\mathbf{u}$  have the Jacobian  $\begin{pmatrix} 1 & 0 \\ 0 & 1 \\ 0 & 0 \end{pmatrix}$ . Any scaling of the third column of  $\mathbf{D}_3$  is actually irrelevant for the statement and proof of the theorem; it cancels out in the evaluation of (40) and (41). It may, however, affect the scaling of deviations from the PDE that occur for positive structuring element radius  $\varrho$ .

With the coordinate transform  $\mathbf{D}_3$ , the proof of the theorem proceeds analogously to the proof of Theorem 1 and relies on the following lemma.

**Lemma 5.** *Let  $\mathbf{u}$  be given as in Theorem 3, with the image domain  $\Omega$  containing the origin  $\mathbf{0} = (0, 0)$  in its interior. Assume that  $\mathbf{D}\mathbf{u}(\mathbf{0}) = \begin{pmatrix} 1 & 0 \\ 0 & 1 \\ 0 & 0 \end{pmatrix}$ . At  $\mathbf{x} = \mathbf{0}$ , one step of Oja median filtering of  $\mathbf{u}$  with the structuring element  $D_\varrho$  then approximates for  $\varrho \rightarrow 0$  an explicit time step of size  $\tau = \varrho^2/24$  of the PDE system*

$$u_t = u_{xx} + 3u_{yy} - 2v_{xy} \quad (42)$$

$$v_t = 3v_{xx} + v_{yy} - 2u_{xy} \quad (43)$$

$$w_t = 2w_{xx} + 2w_{yy}. \quad (44)$$

The proof of this lemma is given in Appendix E. It is based on the result from Lemma 2 for the bivariate Oja median and extends it with a calculation of the  $w_t$  component. In doing the latter, we reformulate the Oja median function into a weighted  $L^1$  median for the feet of altitudes in the triangles, and proceed then analogously to the proof of the three-channel  $L^1$  median result, Lemma 4, where the minimisation condition was evaluated by explicit integration over the structuring element. This approach has been avoided in the other proofs for the Oja median results because in the general Oja median case it turns out extremely tedious, but in the special case considered here it becomes feasible by exploiting a rotational symmetry argument in combination with an integration in polar coordinates similar to the first proof of Lemma 2.

### 3.3.2 Affine Equivariant Transformed $L^1$ Median

Turning to the affine equivariant transformed  $L^1$  median filter, Definition 1 of its space-continuous variant in the bivariate case does not transfer straightforwardly to the situation of three-channel planar images as it uses the inverse of the Jacobian of the input function. For our analysis, we adopt the proceeding from Section 3.3.1 and use the enlarged Jacobian  $\mathbf{D}_3$  with the same scaling convention as in (39). We can then define the filter to be analysed as follows.

**Definition 2** (Space-continuous affine equivariant transformed  $L^1$  median filter for three-channel planar images.). Let a function  $\mathbf{u} : \mathbb{R}^2 \supset \Omega \rightarrow \mathbb{R}^3$  and the structuring element  $D_\varrho$  be given. For each location  $\mathbf{x}_0 \in \Omega$  where  $D\mathbf{u}(\mathbf{x}_0)$  has rank 2, let  $\mathbf{D}_3 = \mathbf{D}_3(\mathbf{x}_0)$  be given as in (39), and transform the function values  $\mathbf{u}(\mathbf{x})$  for  $\mathbf{x} \in \mathbf{x}_0 + D_\varrho$  via  $\hat{\mathbf{u}} = \mathbf{D}_3(\mathbf{x}_0)^{-1}\mathbf{u}$ . Determine the  $L^1$  median  $\hat{\mathbf{u}}^*$  of the data  $\hat{\mathbf{u}}$ . Transform  $\hat{\mathbf{u}}^*$  back to  $\mathbf{u}^*(\mathbf{x}_0) = \mathbf{D}_3(\mathbf{x}_0)\hat{\mathbf{u}}^*$ . The image filter that transfers the input function  $\mathbf{u} : \Omega \rightarrow \mathbb{R}^3$  to the function  $\mathbf{u}^* : \Omega \rightarrow \mathbb{R}^3$  is called affine equivariant transformed  $L^1$  median filter.

*Remark 11.* As in the case of the Oja median, any possible scaling of the third column of  $\mathbf{D}_3$  will be irrelevant for the asymptotic analysis carried out in the following. A caveat arises, however, when a discrete filter based on the transformation–retransformation approach [10, 17, 22] or as implemented in Section 2.3 is used as discrete approximation for variable positive structuring element radius  $\varrho$ . As this discrete procedure just takes the  $\mathbb{R}^3$  input data as samples of a 3D distribution and tries to normalise this distribution, it might introduce a scaling factor that changes with  $\varrho$ . We leave analysis of this difficulty for future work but remark that the results of our numerical experiments in Section 4.1.2 support the validity of the analysis given here.

**Proposition 3.** *Let a three-channel planar image  $\mathbf{u} : \mathbb{R}^2 \supset \Omega \rightarrow \mathbb{R}^3$ ,  $(x, y) \mapsto (u, v, w)$ , be given. At any location where the  $3 \times 2$  matrix  $D\mathbf{u}$  has rank 2, one step of affine equivariant transformed  $L^1$  median filtering of  $\mathbf{u}$  with the structuring element  $D_\varrho$  approximates for  $\varrho \rightarrow 0$  an explicit time step of size  $\tau = \varrho^2/24$  of the PDE system (38) with the coefficient matrices (40)–(41) as stated in Theorem 3.*

The proof of the proposition is analogous to the proof of Theorem 3, using the special case  $u_x = v_y = 1$  of the following lemma. The lemma itself is corrected from [33] and rewritten for the three-channel case.

**Lemma 6** (from [33], corrected). *Let  $\mathbf{u}$  be given as in Proposition 3, with the image domain  $\Omega$  containing the origin  $\mathbf{0} = (0, 0)$  in its interior. Assume that the Jacobian at  $\mathbf{0}$  is of the form  $D\mathbf{u}(\mathbf{0}) = \begin{pmatrix} u_x & 0 \\ 0 & v_y \\ 0 & 0 \end{pmatrix}$  with  $u_x \geq v_y > 0$ . Then one step of  $L^1$  median filtering with the structuring element  $D_\varrho$  approximates for  $\varrho \rightarrow 0$  at  $(x, y)$  an explicit time step of size  $\tau = \varrho^2/6$  of the PDE system consisting of the equations (14), (15), and*

$$w_t = Q_3 \begin{pmatrix} u_x \\ v_y \end{pmatrix} w_{xx} + Q_3 \begin{pmatrix} v_y \\ u_x \end{pmatrix} w_{yy} , \quad (45)$$

where the coefficient function  $Q_3$  is given by

$$Q_3(\lambda) = \frac{3 \iint_{D_1(\mathbf{0})} t^2 / (s^2 + \lambda^2 t^2)^{3/2} ds dt}{\iint_{D_1(\mathbf{0})} 1 / (s^2 + \lambda^2 t^2)^{3/2} ds dt} . \quad (46)$$

*Remark 12.* In the case  $u_x = 1, v_y = 1$ , the coefficients of (45) simplify via  $Q_3(1) = 1/2$  such that one obtains

$$w_t = \frac{1}{2} w_{xx} + \frac{1}{2} w_{yy} , \quad (47)$$

which together with (17) and (18) and after rescaling the time variable by 4 yields (42)–(44). This is the relevant case for the proof of Proposition 3.

## 4 Experimental Validation of the PDEs for Multivariate Median Filtering

This section is focussed at validating the PDE approximation results from Section 3 by numerical experiments.

### 4.1 Simple Example Functions

We start with several experiments on simple example functions in which we compare the individual coefficients of the PDEs for the different variants of multivariate median filters derived in Section 3 with median filtering results for the function values sampled at high resolution.

#### 4.1.1 Bivariate Filters, Case $D\mathbf{u} = \mathbf{I}$

To verify the results on bivariate  $L^1$  and Oja median filtering, we focus first on the case  $D\mathbf{u}(\mathbf{0}) = \mathbf{I}$ , see Remark 3 and Lemma 2.

We discretise sample functions  $u(x, y)$  and  $v(x, y)$  in the structuring element  $D_1(\mathbf{0})$ , i.e. the disc of radius 1 around the origin, with a grid resolution of 0.01 in  $x$  and  $y$  direction, which yields 31 417 sample points. For symmetry reasons, the sample functions are chosen to test only the weights of  $u_{xx}$ ,  $u_{xy}$  and  $u_{yy}$  while leaving  $v(x, y) \equiv y$ . For these input data we compute the  $L^1$  and Oja medians and compare these with the theoretical values given by the right-hand side of (22), (23) with the time step size  $1/24$ . The results can be found in Table 1. The observed deviations in the range of  $1.5 \times 10^{-4}$  between the computed medians and PDE time steps are expectable given the grid resolution.

#### 4.1.2 Three-Channel Planar Image Filters, Isotropic Case

The tests for bivariate filters in the case  $D\mathbf{u} = \mathbf{I}$  from Section 4.1.1 can easily be extended to three-channel planar image filtering by  $L^1$  and 2D Oja medians. Using the same structuring element and sampling grid as before, we sample now  $\mathbb{R}^3$ -valued functions  $(x, y) \mapsto (u, v, w)$  with  $u_x = v_y = 1$ ,  $u_y = v_x = w_x = w_y = 0$ , where we vary single second-order Taylor coefficients away from zero.

Table 1: Validation of the PDE approximation of bivariate  $L^1$  and Oja median filtering in the case  $u_x = v_y = 1$ ,  $u_y = v_x = 0$ , see Remark 3 and Lemma 2. Median values  $(u^*, v^*)$  computed from functions sampled with resolution 0.01 in a disc-shaped structuring element of radius 1 are juxtaposed with the time steps of size  $\tau = 1/24$  of the corresponding PDE system (22), (23). Medians and time steps are scaled by  $10^6$  for more compact representation.

Function		Derivatives			$L^1$ median		Oja median		PDE time step	
$u$	$v$	$u_{xx}$	$u_{xy}$	$u_{yy}$	$10^6 u^*$	$10^6 v^*$	$10^6 u^*$	$10^6 v^*$	$10^6 \tau u_t$	$10^6 \tau v_t$
$x + 0.05x^2$	$y$	0.1	0	0	4 167	0	4 181	0	4 167	0
$x + 0.1xy$	$y$	0	0.1	0	0	-8 364	0	-8 372	0	-8 333
$x + 0.05y^2$	$y$	0	0	0.1	12 479	0	12 479	0	12 500	0

The results shown in Table 2 indicate an accuracy of approximation comparable to the previous case, and thereby confirm the validity of the approximation results from Lemma 5 and Lemma 6 (with  $u_x = v_y = 1$ ). We have omitted test cases where only second derivatives of  $u$  and  $v$  were varied, because in these cases results were identical to the pure bivariate case.

#### 4.1.3 Nonlinear Dampening

Referring to our discussion in Section 3.1.4 regarding the behaviour of multivariate median filters and the corresponding PDEs for structuring elements  $D_\varrho$  of nonvanishing radius  $\varrho$ , we turn to check by an additional numerical experiment how an increase of the second derivatives away from zero effects the median.

To this end, we compute bivariate Oja medians, again with a structuring element of radius  $\varrho = 1$  discretised with grid resolution 0.01, for functions with increasing values of the three second partial derivatives  $u_{xx}$ ,  $u_{yy}$ ,  $v_{xy}$  occurring on the right-hand side of (22). The underlying functions are

- $u = x + \frac{1}{2}sx^2$ ,  $v = y$  for the test of  $u_{xx}$ ,
- $u = x + \frac{1}{2}sy^2$ ,  $v = y$  for the test of  $u_{yy}$ , and
- $u = x$ ,  $v = y - sxy$  for the test of  $v_{xy}$ ,

where  $s$  is varied from 0 to 2.5.

Figure 7 shows the  $u$  components of the resulting Oja medians dependent on the values of  $s$ . For  $s$  close to zero they increase linearly with the ascents predicted by (22). Regarding  $u_{xx}$  and  $u_{yy}$ , the median values follow this linear ascent closely, within 10 % tolerance, up to  $s \approx 1$ , after which the values grow rapidly faster in the  $u_{xx}$  case, and are dampened in the  $u_{yy}$  case.

In contrast, in the  $v_{xy}$  case the deviation from linear behaviour starts much earlier, leading to more than 10 % deviation already for  $s \approx 0.6$ , with the growth of the median rapidly being

Table 2: Validation of the PDE approximation of  $L^1$  and 2D Oja median filtering of three-channel planar image data in the case  $u_x = v_y = 1$ ,  $u_y = v_x = w_x = w_y = 0$ . Median values ( $u^*$ ,  $v^*$ ,  $w^*$ ) computed from functions sampled with resolution 0.01 in a disc-shaped structuring element of radius 1 are juxtaposed with the time steps of size  $\tau = 1/24$  of the corresponding PDE system (42)–(44). Medians and time steps are scaled by  $10^6$  for more compact representation.

$u$	Function		Nonzero second derivatives	$L^1$ median			Oja median			PDE time step		
	$v$	$w$		$10^6 u^*$	$10^6 v^*$	$10^6 w^*$	$10^6 u^*$	$10^6 v^*$	$10^6 w^*$	$10^6 \tau u_t$	$10^6 \tau v_t$	$10^6 \tau w_t$
$x$	$y$	$0.05x^2$	$w_{xx} = 0.1$	0	0	8 401	0	0	8 390	0	0	8 333
$x$	$y$	$0.1xy$	$w_{xy} = 0.1$	0	0	0	0	0	0	0	0	0
$x$	$y$	$0.05y^2$	$w_{yy} = 0.1$	0	0	8 401	0	0	8 390	0	0	8 333
$x + 0.05x^2$	$y$	$0.05x^2$	$\begin{cases} u_{xx} = 0.1 \\ w_{xx} = 0.1 \end{cases}$	4 180	0	8 405	4 197	0	8 391	4 167	0	8 333
$x + 0.05x^2$	$y$	$0.1xy$	$\begin{cases} u_{xx} = 0.1 \\ w_{xy} = 0.1 \end{cases}$	4 172	0	0	4 150	0	0	4 167	0	0
$x + 0.05x^2$	$y$	$0.05y^2$	$\begin{cases} u_{xx} = 0.1 \\ w_{yy} = 0.1 \end{cases}$	4 175	0	8 401	4 195	0	8 389	4 167	0	8 333

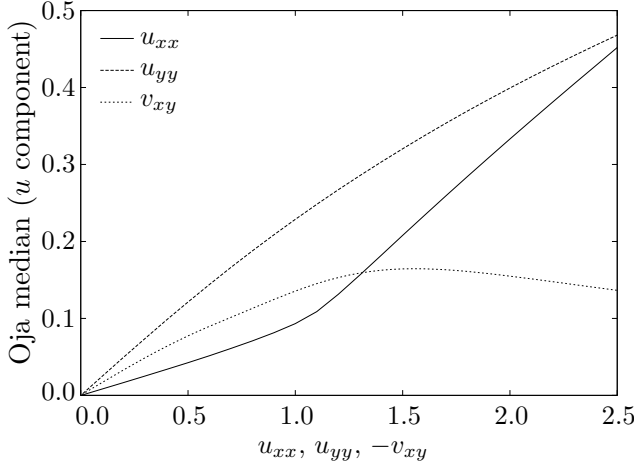


Figure 7: Nonlinear response of bivariate Oja median filter for fixed structuring element radius  $\varrho = 1$  to Taylor coefficients  $u_{xx}$ ,  $u_{yy}$ ,  $v_{xy}$ , where  $D\mathbf{u} = \mathbf{I}$ .

dampened above this level. For large  $s$ , the effect of the coefficient  $v_{xy}$  on the median even starts to decrease. The response of the median value to  $v_{xy}$  confirms the inherent nonlinear dampening effect of the median filter procedure.

#### 4.1.4 A More Complex Bivariate Example

To demonstrate the validity of the PDE approximation results of Proposition 1, Theorem 1, and Corollary 1 also away from the special case  $D\mathbf{u} = \mathbf{I}$ , we consider a simple bivariate example function given by

$$u(x, y) = x^2, \quad v(x, y) = \sqrt{x^2 + y^2}. \quad (48)$$

Level sets of  $u$  and  $v$  for this function in the range  $[0, 1] \times [0, 1]$  are depicted in Figure 8. In this figure, also seven test locations a–g are depicted together with structuring elements of radius  $\varrho = 0.1$  for which we compare in the following median filter values with time steps  $(\tau u_1, \tau v_1)$  of the respective PDE counterparts.

We start with the  $L^1$  median and the PDE (8)–(11) from Proposition 1. Time steps  $(\tau u_t, \tau v_t)$  of the PDE (8) at the locations a–g were computed analytically, using numeric integration for the integral values  $Q_1(\lambda)$  and  $Q_2(\lambda)$ . The time step size for (8) was  $\tau = \varrho^2/6 = 0.001667$ . For the computation of  $L^1$  medians, the structuring elements of radius  $\varrho$  around locations a–g were sampled at grid resolution 0.001 resulting in approx. 31 000 sample points for each location. From their function values  $(u, v)$  the  $L^1$  median  $(u^*, v^*)$  was computed by the gradient descent method. For comparison with the PDE time step the input function value of the midpoint was subtracted. Table 3 shows PDE time steps, the corresponding median filter updates  $u^* - u$ ,  $v^* - v$  and the relative errors (in Euclidean norm) with respect to the PDE time steps, i.e.  $|(u^* - u - \tau u_t, v^* - v - \tau v_t)|/|\tau u_t, \tau v_t|$ .

For the Oja median, we proceed analogously, with the analytically computed PDE time steps of (19), Oja median filter updates and their relative errors being shown in Table 4. The time step size for (19) was  $\tau = \varrho^2/24 = 0.000417$ . The Oja median values were computed using the gradient descent method. Moreover, Table 4 contains results of the affine equivariant transformed  $L^1$  median which according to Corollary 1 approximates the same PDE.

In Table 3, the results for locations c–g show relative errors below 3%, which are reasonable given the structuring element radius  $\varrho = 0.1$  and the grid resolution. The approximation at locations a and b is less accurate. At these locations, the gradients of  $u$  and  $v$  are almost

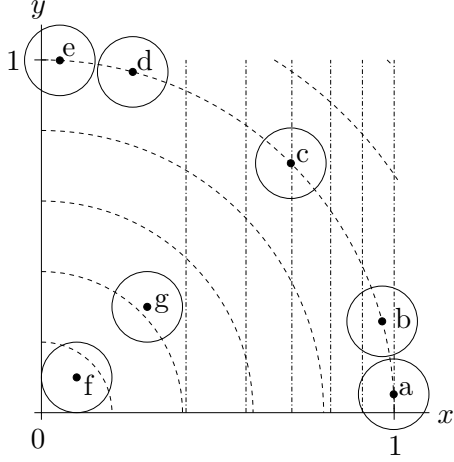


Figure 8: Example function  $(u, v) = (x^2, \sqrt{x^2 + y^2})$  used to demonstrate PDE approximation of bivariate median filters. Dot-dashed lines are level lines  $u = \text{const}$ , dashed lines are level lines  $v = \text{const}$ . Points a–g are the sample locations for which numerical results are given in Table 4, surrounded by their structuring elements as solid circles.

aligned and not close to zero, making the Jacobian  $D\mathbf{u}$  ill-conditioned. Locations e and f where the gradient  $\nabla u$  is small and  $D\mathbf{u}$  therefore also ill-conditioned, create less problems for the approximation.

The results in Table 4 show that the approximation of the PDE (19) by both the Oja median and the transformed  $L^1$  median is fairly accurate, with relative errors of less than 2%, at locations b, c, d and g where  $\det D\mathbf{u}$  is sufficiently different from zero. Larger discrepancies are observed for locations a, e, and f which are closer to the coordinate axes. Note that on the  $x$  axis,  $D\mathbf{u}$  becomes singular due to coinciding gradient directions for  $u$  and  $v$ , while on the  $y$  axis it does so due to the vanishing of  $\nabla u$ .

A comparison of Tables 3 and 4 underlines that the standard  $L^1$  median on one hand and the Oja median and transformed  $L^1$  median on the other hand indeed differ substantially. For their very similar results in the tests of Section 4.1.1 it was decisive that the case  $D\mathbf{u} = \mathbf{I}$  was tested there. In contrast, for our test function here the Jacobian is far away from the unit matrix, not only in locations a, e, f where it is near the degenerate case but also in the fairly regular locations b–d and g.

A close look at Table 4 also makes clear that, although they approximate the same PDE, the Oja median filter and affine equivariant transformed  $L^1$  median filter are not identical. An analysis of the higher order terms neglected in the PDE approximation analysis of Section 3 could shed more light on these differences.

#### 4.1.5 Three-Channel Volume Images, Case $D\mathbf{u} = \mathbf{I}$

For the three-channel case, we consider the case  $D\mathbf{u}(\mathbf{0}) = \mathbf{I}$  as treated in Lemmas 3 and 4.

We discretise sample functions  $u(x, y, z)$ ,  $v(x, y, z)$ ,  $w(x, y, z)$  in the structuring element  $B_1(\mathbf{0})$ , i.e. the ball of radius 1 around the origin, with a grid resolution of 0.15 in the  $x$ ,  $y$  and  $z$  directions, which yields 1237 sample points. The coarser resolution compared to Section 4.1.1 is a tribute to the unfavourable computational complexity of our three-channel Oja median computation.

Again, it suffices for symmetry reasons to consider sample functions that test only the weights of the second derivatives of  $u$  while leaving  $v(x, y, z) \equiv y$  and  $w(x, y, z) \equiv z$ . For these input data we compute the Oja and  $L^1$  medians and compare these with the theoretical values given by the right-hand side of (35)–(37) with the time step size  $1/20$ . The results can be found in Table 5. The observed deviations in the range of  $2 \times 10^{-4}$  between the computed

Oja medians and PDE time steps are expectable given the grid resolution. For the  $L^1$  median, larger deviations up to  $8 \times 10^{-4}$  are observed. However, doing the same computation with a finer sampling grid – which is computationally feasible with our implementation of the  $L^1$  median but not for the Oja median – yields values also for the  $L^1$  median that match the time step of (35)–(37) closely, thereby confirming also the asymptotic equivalence of the Oja and affine equivariant transformed  $L^1$  filter for three-channel volume images.

Table 3: Comparison of analytically computed time steps ( $\tau u_t, \tau v_t$ ) of the PDE (8)–(11) with numerical computation of the  $L^1$  median ( $u^*, v^*$ ) for the function  $(u, v) = (x^2, \sqrt{x^2 + y^2})$ . To compute  $(u^*, v^*)$ , the structuring element of radius  $\varrho = 0.1$  was sampled using a grid with spatial mesh size  $h = 0.001$ , generating about 31 000 data points. The time step size for (8) was chosen as  $\tau = \varrho^2/6 = 0.001667$ . Medians and time steps are scaled by  $10^6$  for more compact representation.

	Location		Function value		PDE time step		$L^1$ median		
	$x_0$	$y_0$	$u$	$v$	$10^6 \tau u_t$	$10^6 \tau v_t$	$10^6(u^* - u)$	$10^6(v^* - v)$	rel. error
a)	0.9986	0.0523	0.9973	1.0000	320	1 045	232	1 026	8.24 %
b)	0.9659	0.2588	0.9330	1.0000	574	754	539	738	4.06 %
c)	0.7071	0.7071	0.5000	1.0000	942	628	926	613	1.94 %
d)	0.2588	0.9659	0.0670	1.0000	1 338	1 095	1 337	1 083	0.70 %
e)	0.0523	0.9986	0.0027	1.0000	2 120	1 579	2 197	1 562	2.98 %
f)	0.1000	0.1000	0.0100	0.1414	2 098	10 715	2 071	10 446	2.48 %
g)	0.3000	0.3000	0.0900	0.4243	1 657	2 593	1 647	2 577	0.61 %

Table 4: Comparison of numerical computed Oja median and transformed  $L^1$  median with analytically computed time steps ( $\tau u_t, \tau v_t$ ) of the PDE (19)–(21) for the function  $(u, v) = (x^2, \sqrt{x^2 + y^2})$ . To compute medians ( $u^*, v^*$ ), the structuring element of radius  $\varrho = 0.1$  was sampled using a grid with spatial mesh size  $h = 0.001$ , generating about 31 000 data points. The time step size for (19) was chosen as  $\tau = \varrho^2/24 = 0.000417$ . Medians and time steps are scaled by  $10^6$  for more compact representation.

	Location		Function val.		PDE time step		Oja median			Transformed $L^1$ median		
	$x_0$	$y_0$	$u$	$v$	$\tau u_t$ $\times 10^6$	$\tau v_t$ $\times 10^6$	$(u^* - u)$ $\times 10^6$	$(v^* - v)$ $\times 10^6$	rel. error	$(u^* - u)$ $\times 10^6$	$(v^* - v)$ $\times 10^6$	rel. error
a)	0.9986	0.0523	0.9973	1.0000	2 495	417	1 896	538	24.16 %	2 138	637	16.58 %
b)	0.9659	0.2588	0.9330	1.0000	2 388	417	2 355	417	1.36 %	2 355	413	1.37 %
c)	0.7071	0.7071	0.5000	1.0000	1 667	417	1 650	404	1.25 %	1 652	403	1.19 %
d)	0.2588	0.9659	0.0670	1.0000	945	417	943	407	0.99 %	948	409	0.83 %
e)	0.0523	0.9986	0.0027	1.0000	838	417	920	448	9.37 %	1 056	512	25.41 %
f)	0.1000	0.1000	0.0100	0.1414	1 667	2 946	1 587	3 668	21.46 %	1 689	3 751	23.79 %
g)	0.3000	0.3000	0.0900	0.4243	1 667	982	1 654	1 009	1.55 %	1 666	1 003	1.09 %

## 4.2 Iterated Median Filters and PDE Evolution

In our final experiment, we return to the filtering of RGB images and make now the transition to iterated median filtering. In these experiments, a numerical scheme for the PDE (38)–(41) is used. We start therefore with a brief description of this scheme.

### 4.2.1 Numerical Approximation of the Affine Equivariant Median PDE

We assume that the three-channel input image  $\mathbf{f}$  for the PDE (38)–(41) is sampled on an isotropic regular grid with spatial step size  $h$  in the  $x$  and  $y$  directions, and denote by  $\mathbf{f}_{i,j}$  the intensity triple at pixel  $(i, j)$ . We will compute by an explicit finite-difference scheme a sequence  $(\mathbf{u}^k)$  of filtered images that approximate the PDE at evolution times  $k\tau$  with time step size  $\tau$ , with  $\mathbf{u}^0 \equiv \mathbf{f}$ . By  $\mathbf{u}_{i,j}^k = (u_{i,j}^k, v_{i,j}^k, w_{i,j}^k)^\top$  we denote the value of pixel  $(i, j)$  in the  $k$ -th iteration.

In computing  $\mathbf{u}_{i,j}^{k+1}$  from the previous image  $\mathbf{u}^k$  we use the pixels  $\mathbf{u}_{i',j'}^k$  from the  $3 \times 3$  patch  $\mathcal{P}_{i,j}$  given by  $i' \in \{i-1, i, i+1\}$  and  $j' \in \{j-1, j, j+1\}$ .

The numerical scheme transforms the input data  $\mathbf{u}$  within each patch  $\mathcal{P}_{i,j}$  by an orthogonal transform  $\mathbf{u} = (u, v, w) \mapsto \hat{\mathbf{u}} = (\hat{u}, \hat{v}, \hat{w})$  of the values and determining a new orthogonal basis  $(\boldsymbol{\eta}, \boldsymbol{\xi})$  in the  $(x, y)$  plane such that  $\hat{u}_{\boldsymbol{\eta}}$  and  $\hat{v}_{\boldsymbol{\xi}}$  are the only nonzero entries of the Jacobian  $D_{\boldsymbol{\eta}\boldsymbol{\xi}}\hat{\mathbf{u}}$  w.r.t. the new coordinates at pixel  $(i, j)$ . The PDE to be approximated then reads

$$\begin{pmatrix} \hat{u}_t \\ \hat{v}_t \\ \hat{w}_t \end{pmatrix} = \underbrace{\begin{pmatrix} \hat{u}_{xx} + \hat{u}_{yy} \\ \hat{v}_{xx} + \hat{v}_{yy} \\ \hat{w}_{xx} + \hat{w}_{yy} \end{pmatrix}}_{\mathbf{z}_1} + 2 \underbrace{\begin{pmatrix} \hat{u}_{\boldsymbol{\xi}\boldsymbol{\xi}} \\ \hat{v}_{\boldsymbol{\eta}\boldsymbol{\eta}} \\ 0 \end{pmatrix}}_{\mathbf{z}_2} - 2 \underbrace{\begin{pmatrix} \hat{u}_{\boldsymbol{\eta}}\hat{v}_{\boldsymbol{\eta}\boldsymbol{\xi}}/\hat{v}_{\boldsymbol{\xi}} \\ \hat{v}_{\boldsymbol{\xi}}\hat{u}_{\boldsymbol{\eta}\boldsymbol{\xi}}/\hat{u}_{\boldsymbol{\eta}} \\ 0 \end{pmatrix}}_{\mathbf{z}_3}. \quad (49)$$

Herein, the first contribution  $\mathbf{z}_1$  is approximated by central differences even in the original  $(x, y)$  coordinates. The second contribution  $\mathbf{z}_2$  is approximated by central differences in the  $(\boldsymbol{\eta}, \boldsymbol{\xi})$  basis. For the third contribution  $\mathbf{z}_3$ , such a discretisation would be unstable and also unable to cope with locations where  $\hat{u}_{\boldsymbol{\eta}}$  or  $\hat{v}_{\boldsymbol{\xi}}$  vanishes. Therefore, two stabilisations are used. First, the weight factor  $\hat{v}_{\boldsymbol{\eta}\boldsymbol{\xi}}/\hat{v}_{\boldsymbol{\xi}}$  is approximated by the regularised expression  $R_v := \hat{v}_{\boldsymbol{\eta}\boldsymbol{\xi}}\hat{v}_{\boldsymbol{\xi}}/(\hat{v}_{\boldsymbol{\xi}}^2 + \varepsilon)$  with a fixed numerical regularisation parameter  $\varepsilon$  using central differences in the

Table 5: Validation of the PDE approximation of three-channel Oja median filtering in the case  $D\mathbf{u} = \mathbf{I}$ , see Lemma 3, including for comparison also the  $L^1$  median. Median values  $(u^*, v^*, w^*)$  computed from functions sampled with resolution 0.15 in a ball-shaped structuring element of radius 1 are juxtaposed with the time steps of size  $\tau = 1/20$  of the corresponding PDE system. Medians and time steps are scaled by  $10^4$  for more compact representation.

Function		Nonzero 2 <sup>nd</sup> derivatives	$L^1$ median			Oja median			PDE time step		
$u$	$v \ w$		$10^4 u^*$	$10^4 v^*$	$10^4 w^*$	$10^4 u^*$	$10^4 v^*$	$10^4 w^*$	$10^4 \tau u_t$	$10^4 \tau v_t$	$10^4 \tau w_t$
$x + 0.05x^2$	$y \ z$	$u_{xx} = 0.1$	42	0	0	48	0	0	50	0	0
$x + 0.1xy$	$y \ z$	$u_{xy} = 0.1$	0	-42	0	1	-48	0	0	-50	0
$x + 0.1xz$	$y \ z$	$u_{xz} = 0.1$	0	0	-42	1	0	-48	0	0	-50
$x + 0.05y^2$	$y \ z$	$u_{yy} = 0.1$	93	0	0	99	0	0	100	0	0
$x + 0.1yz$	$y \ z$	$u_{yz} = 0.1$	0	0	0	0	0	0	0	0	0
$x + 0.05z^2$	$y \ z$	$u_{zz} = 0.1$	93	0	0	99	0	0	100	0	0

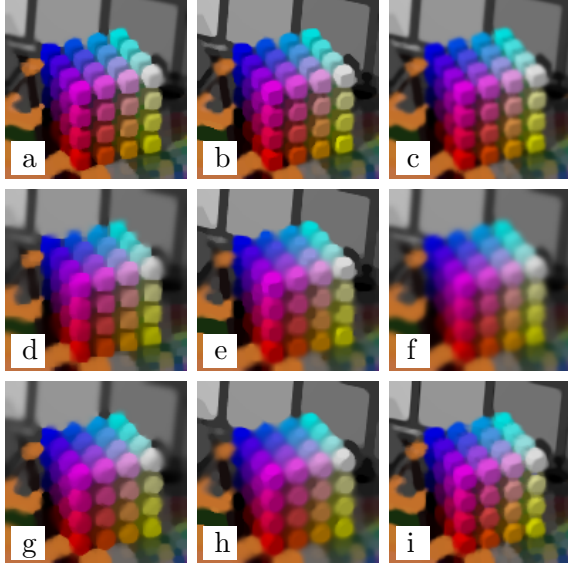


Figure 9: Comparison of iterated median filtering of the *Colors* test image from Figure 5 (a) using affine equivariant multivariate medians and PDE filtering of the same image. **Top row, left to right:** (a) 2D Oja median,  $\varrho = 2$ , with input regularisation, 3 iterations. – (b) Affine equivariant transformed  $L^1$  median,  $\varrho = 2$ , 3 iterations. – (c) PDE (38), explicit finite difference scheme, 10 iterations with time step size  $\tau = 0.05$ . – **Middle row, left to right:** (d) 2D Oja median,  $\varrho = 2$ , with input regularisation, 9 iterations. – (e) Affine equivariant transformed  $L^1$  median,  $\varrho = 2$ , 9 iterations. – (f) PDE (38), explicit finite difference scheme, 30 iterations with time step size  $\tau = 0.05$ . – **Bottom row, left to right:** (g) 2D Oja median,  $\varrho = 3$ , with input regularisation, 4 iterations. – (h) Affine equivariant transformed  $L^1$  median,  $\varrho = 3$ , 4 iterations. – (i) PDE (38), explicit finite difference scheme, 30 iterations with time step size  $\tau = 0.05$ , with heuristic anti-diffusion to compensate for numerical dissipation.

numerator and a combination of minmod-stabilised one-sided differences in the denominator; a similar expression  $R_u$  is used for  $\hat{u}_{\eta\xi}/\hat{u}_{\eta}$ . Second, the factor  $u_{\eta}$  in the first component is discretised in an upwind way by choosing a one-sided difference according to the sign of  $R_v$ ; analogously for  $v_{\xi}$  in the second component.

For utmost explicitness, the scheme is stated as a detailed algorithm in Appendix F.

#### 4.2.2 Image Filtering Experiment

Using the algorithms described so far in the paper, we compute iterated median filters of the RGB image from Figure 5 (a) and their supposed PDE evolution counterpart. Results are shown in Figure 9.

In the first row, the filter parameters of the 2D Oja median filter and the affine equivariant transformed  $L^1$  median filter are adjusted such as to correspond to an evolution time  $T = 0.5$  of the PDE system (38). To this end, a structuring element of radius  $\varrho = 2$  is used, and 3 iterations of both median filters carried out, see the results in Figure 9 (a) and (b). In frame (c), the result from the numerical evaluation of the PDE is shown. With time step size  $\tau = 0.05$  and 10 iterations this represents also the evolution time  $T = 0.5$ .

In the second row of Figure 9, frames (d)–(f), the same filters are shown for an evolution time of  $T = 1.5$ , i.e. 9 median iterations and 30 time steps, respectively. Regarding the structure simplification by rounding contours etc., the results for the same evolution time are largely comparable, with the transformed  $L^1$  median featuring the sharpest preservation of edges (with exception of a few structures where the Oja median result appears sharper). The PDE results are visibly more blurred. It can be conjectured that this blur is not intrinsic to the PDE but to the numerical dissipation that usually comes with explicit finite difference schemes for curvature-based PDEs.

Figure 9 (g) and (h) show median filtering results for the same evolution time  $T = 1.5$ , but this time realised with structuring element radius  $\varrho = 3$  and 4 iterations. The sharpness and overall degree of structure simplification is fairly comparable with frames (d) and (e), which confirms that indeed the progress of the filtering process scales with  $\varrho^2$  as suggested by the approximation theorem. Some corners are being rounded more pronouncedly with the larger structuring element (see for example the grey tiles in the background).

Based on the assumption that the higher amount of blur in the PDE results so far is caused by numerical dissipation inherent to the finite-difference discretisation, one might think of modifying the numerical scheme by sharpening terms that compensate for this dissipation, see the *flux-corrected transport* approach established in [7] and used in image processing e.g. in [8] for hyperbolic PDEs. Of course, a well-founded modification of the numerical scheme from Section 4.2.1 would require a detailed analysis of its approximation errors, which we cannot provide at this point. However, the PDE under consideration offers a simple way to test this idea on a heuristic level. To see this, note that the PDE (49) includes the isotropic (forward) diffusion term  $\mathbf{z}_1 = \hat{\mathbf{u}}_{xx} + \hat{\mathbf{u}}_{yy}$ . Let us therefore introduce inverse linear diffusion  $-\lambda \mathbf{z}_1$  with an anti-diffusion weight  $\lambda > 0$  as a heuristic flux correction. This is tantamount to just reducing the weight of  $\mathbf{z}_1$  in (49) from 1 to  $1 - \lambda$ . As long as  $\lambda \leq 1$ , the net linear diffusion  $(1 - \lambda)\mathbf{z}_1$  is forward diffusion, thus not harming the stability of the numerical scheme. In Figure 9 (i) we present the result of filtering the test image with the so-modified scheme with  $\lambda = 1$ , i.e. completely suppressing  $\mathbf{z}_1$ . The filtered image is fairly similar to the median filtering results in frames (e) and (h) regarding sharpness and contour simplification. Regarding those details which are filtered more pronouncedly in frames (g) and (h) than in (d) and (e), visual inspection places the modified PDE result (i) closer to (d) and (e), which is natural given that the approximation of the PDE by median filtering is asymptotic for  $\varrho \rightarrow 0$ .

## 5 Summary and Outlook

In this paper, we have analysed multivariate median filters in a space-continuous setting with emphasis on their asymptotic behaviour. We have considered  $L^1$ , 2D and 3D Oja median filters and affine equivariant transformed (transformation–retransformation)  $L^1$  median filters for bivariate planar images, three-channel volume images and three-channel planar images. In all these cases, we have derived PDEs approximated by multivariate median filters in the limit for vanishing radius of the structuring element. We have verified these PDE approximation statements by numerical experiments.

An important outcome of our analysis is that the Oja median filter and the affine equivariant transformed  $L^1$  median filter are asymptotically equivalent in relevant settings. The iterated Oja median filter, the transformed  $L^1$  median filter and the corresponding PDE can therefore be considered as different approximations to the same kind of ideal *affine equivariant median filter*.

Future work on the theoretical side might be directed at obtaining a more general form of the approximation statements, such as uniform representations of PDEs for median filtering of  $n$ -dimensional data over  $m$ -dimensional domains, including affine equivariant transformed  $L^1$  and different  $k$ -dimensional Oja medians. The numerical scheme from Section 4.2.1, while working in experiments, still lacks a detailed stability analysis. As pointed out in Section 4.2.2, it would also be of interest to analyse the numerical dissipation in this scheme by studying the approximation errors of its finite difference approximations, in order to formulate a theo-

retically well-founded corrected scheme instead of the heuristic anti-diffusion approach used in Figure 9 (i).

Regarding the implementation of multivariate median filtering, more efficient algorithms for Oja median filtering should be investigated along the lines sketched in Section 2.1. In the light of the above-mentioned asymptotic equivalence of affine equivariant multivariate medians, however, using the transformation–retransformation  $L^1$  median appears as a viable alternative.

Finally, the results of the present paper may open different avenues to a broader application of multivariate median filters in image processing. On one hand, based on a proper theoretical understanding of its effect, affine equivariant (Oja or transformed  $L^1$ ) median filtering can be studied in practical image processing applications to find out more about its practical advantages or disadvantages. On the other hand, although the PDE approximated by affine equivariant median filters is not quite as simple as the mean curvature motion equation approximated by univariate median filtering, its geometric contributions are also explicit enough to raise the expectation that medians can be used as a building block in nonstandard numerical approximations of multivariate curvature-based PDEs.

On a wider horizon, a further topic of interest for future research is whether also other multivariate median concepts from statistical literature, which generalise other properties of the univariate median than the distance sum minimisation, can be incorporated into the theoretical framework and made useful for image processing.

## A First Proof of Lemma 2

We restate here the proof from [31] with slight modifications and additional details.

The Taylor expansion of  $(u, v)$  up to second order around  $(0, 0)$  reads as

$$\begin{pmatrix} u(x, y) \\ v(x, y) \end{pmatrix} = \begin{pmatrix} x \\ y \end{pmatrix} + \begin{pmatrix} \alpha_1 x^2 + \beta_1 xy + \delta_1 y^2 \\ \alpha_2 x^2 + \beta_2 xy + \delta_2 y^2 \end{pmatrix}, \quad (50)$$

where the coefficients are given by derivatives of  $u, v$  at  $(x, y) = (0, 0)$  as

$$\alpha_1 = \frac{1}{2}u_{xx}(0, 0), \quad \beta_1 = u_{xy}(0, 0), \quad \delta_1 = \frac{1}{2}u_{yy}(0, 0), \quad (51)$$

$$\alpha_2 = \frac{1}{2}v_{xx}(0, 0), \quad \beta_2 = v_{xy}(0, 0), \quad \delta_2 = \frac{1}{2}v_{yy}(0, 0). \quad (52)$$

Restating the definition of Oja’s simplex median for continuous data sets with density function  $f(u, v)$ , we seek the point  $M := (u^*, v^*)$  which minimises the integral over all areas of triangles  $MAB$  with  $A = (u_1, v_1)$  and  $B = (u_2, v_2)$  with  $(u_1, v_1) = (u(x_1, y_1), v(x_1, y_1))$ ,  $(u_2, v_2) = (u(x_2, y_2), v(x_2, y_2))$ ,  $(x_1, y_1), (x_2, y_2) \in D_\varrho(0, 0)$ , weighted with the density  $f(u_1, v_1)f(u_2, v_2)$ .

For each triangle  $MAB$ , the negative gradient of its area as function of  $M$  is a force vector  $\frac{1}{2}F_{M;AB}$  where  $F_{M;AB}$  is perpendicular to  $AB$  with a length proportional to the length  $|AB|$ , see Figure 10. Assuming that  $MAB$  is positively oriented, this vector equals  $(v_2 - v_1, -u_2 + u_1)$ .

Sorting the pairs  $(A, B)$  by the orientation angles  $\varphi$  of the lines  $F_{M;AB}$ , we see that the minimisation condition for the Oja median can be expressed as

$$\Phi(u^*, v^*) = \frac{1}{4} \int_0^{2\pi} \begin{pmatrix} \cos \varphi \\ \sin \varphi \end{pmatrix} F(u^*, v^*, \varphi) d\varphi = 0. \quad (53)$$

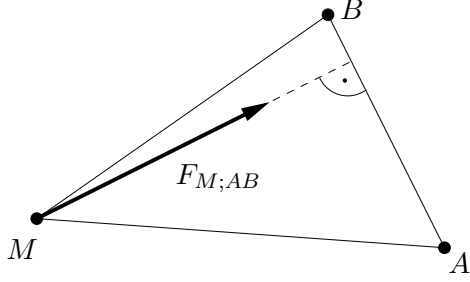


Figure 10: Anti-gradient vector  $F_{M;AB}$  for the area of a triangle  $MAB$  with variable point  $M$ . From [31].

Here,  $F(\varphi)$  is essentially the resultant of all forces  $F_{M;AB}$  for which the line  $AB$  intersects the ray from  $M$  in direction  $(\cos \varphi, \sin \varphi)$  perpendicularly. Each force  $F_{M;AB}$  is weighted with the combined density  $f(A)f(B) = f(u_1, v_1)f(u_2, v_2)$ .

The factor  $1/4$  in front of the integral (53) combines the factor  $1/2$  from the force vector mentioned above with another factor  $1/2$  to compensate that each triangle  $MAB$  enters the integral twice (once as  $MAB$  and once as  $MBA$ , where the orientation factor cancels by squaring). Note that in [31] the integral was stated differently, integrating only over the triangles with positive orientation.

Moreover,  $u^*, v^*$  will be of order  $\mathcal{O}(\varrho)$  (in fact, even  $\mathcal{O}(\varrho^2)$ ). Thus,  $(u^*, v^*)$  can be expressed up to higher order terms via linearisation as

$$\begin{pmatrix} u^* \\ v^* \end{pmatrix} = -(\mathbf{D}\Phi(0,0))^{-1}\Phi(0,0). \quad (54)$$

We therefore turn now to derive an expression for  $F(0,0,\varphi)$ . Considering first  $\varphi = 0$ , this means that all point pairs  $(A,B)$  in the  $u$ - $v$  right half-plane with  $u_1 = u_2$  contribute to  $F(0,0,0)$ , yielding

$$F(0,0,0) = \int_0^{+\infty} \int_{-\infty}^{+\infty} \int_{-\infty}^{+\infty} f(u, v_1)f(u, v_2)(v_2 - v_1)^2 dv_2 dv_1 du. \quad (55)$$

Note that the factor  $(v_2 - v_1)$  occurs squared in the integrand. One factor  $|v_2 - v_1|$  originates from the length of the triangle baseline  $AB$ . The second factor  $|v_2 - v_1|$  results from the fact that we have organised in (53), (55) an integration over point pairs  $(A,B)$  in the plane using a polar coordinate system similar to a Radon transform;  $v_2 - v_1$  arises as the Jacobian of the corresponding coordinate transform from Cartesian to Radon coordinates. The derivatives of  $F(u^*, v^*, 0)$  with regard to the coordinates of  $M$  are

$$F_{u^*}(0,0,0) = - \int_{-\infty}^{+\infty} \int_{-\infty}^{+\infty} f(0, v_1)f(0, v_2)(v_2 - v_1)^2 dv_2 dv_1, \quad (56)$$

$$F_{v^*}(0,0,0) = 0. \quad (57)$$

Forces  $F(0,0,\varphi)$  and their derivatives for arbitrary angles  $\varphi$  will later be obtained from (55), (56), (57) by rotating the  $u, v$  coordinates accordingly.

For the median of the values  $(u, v)$  within a  $\varrho$ -neighbourhood of  $(x, y) = (0, 0)$ , the density  $f(u, v)$  is zero outside of an  $\mathcal{O}(\varrho)$ -neighbourhood of  $(0, 0)$ , allowing to limit the indefinite integrals from (55) to the intervals  $u \in [0, \bar{u}]$ ,  $v_1, v_2 \in [\underline{v}(u), \bar{v}(u)]$  such that

$$F(0,0,0) = \int_0^{\bar{u}} \int_{\underline{v}(u)}^{\bar{v}(u)} \int_{\underline{v}(u)}^{\bar{v}(u)} f(u, v_1)f(u, v_2)(v_2 - v_1)^2 dv_2 dv_1 du. \quad (58)$$

Expanding  $(v_2 - v_1)^2 = v_2^2 - 2v_1v_2 + v_1^2$ , (58) can be further decomposed into

$$F(0, 0, 0) = \int_0^{\bar{u}} (2J_2(u)J_0(u) - 2J_1(u)^2) du \quad (59)$$

where

$$J_k(u) := \int_{\underline{v}(u)}^{\bar{v}(u)} f(u, v) v^k dv \quad (60)$$

for  $k = 0, 1, 2$ . Similarly, (56) yields

$$F_{u^*}(0, 0, 0) = -(2J_2(0)J_0(0) - 2J_1(0)^2). \quad (61)$$

To compute  $F(0, 0, 0)$  and  $F_{u^*}(0, 0, 0)$ , we write them as functions of the coefficients of (50), i.e.  $F(0, 0, 0) =: G(\alpha_1, \beta_1, \delta_1, \alpha_2, \beta_2, \delta_2)$  and  $F_{u^*}(0, 0, 0) =: H(\alpha_1, \beta_1, \delta_1, \alpha_2, \beta_2, \delta_2)$ .

We will linearise  $G$  and  $H$  around the point  $(\alpha_1, \beta_1, \delta_1, \alpha_2, \beta_2, \delta_2) = \mathbf{0}$  that represents the linear function  $(u(x, y), v(x, y)) = (x, y)$ . To justify this linearisation, remember that we are interested in the limit  $\varrho \rightarrow 0$ , such that only the terms of lowest order in  $\varrho$  matter. Cross-effects between the different coefficients occur only in higher order terms. Denoting from now on by  $\doteq$  equality up to higher order terms, we have therefore

$$G \doteq G^0 + G_{\alpha_1}^0 \alpha_1 + G_{\beta_1}^0 \beta_1 + G_{\delta_1}^0 \delta_1 + G_{\alpha_2}^0 \alpha_2 + G_{\beta_2}^0 \beta_2 + G_{\delta_2}^0 \delta_2, \quad (62)$$

$$H \doteq H^0 + H_{\alpha_1}^0 \alpha_1 + H_{\beta_1}^0 \beta_1 + H_{\delta_1}^0 \delta_1 + H_{\alpha_2}^0 \alpha_2 + H_{\beta_2}^0 \beta_2 + H_{\delta_2}^0 \delta_2 \quad (63)$$

where  $G^0$ ,  $G_{\alpha_1}^0$  etc. are short for  $G(\mathbf{0})$ ,  $G_{\alpha_1}(\mathbf{0})$  etc.

To compute  $G^0$  and  $H^0$ , we insert into (55) the bounds  $\bar{u} = \varrho$ ,  $\bar{v}(u) = \sqrt{\varrho^2 - u^2}$ ,  $\underline{v}(u) = -\bar{v}(u)$ . The density becomes constant within the region defined by  $\bar{u}$ ,  $\underline{v}(u)$  and  $\bar{v}(u)$ , with  $f(u, v) = 1$ . Thus we have

$$J_2(u) = \frac{2}{3}(\varrho^2 - u^2)^{3/2}, \quad (64)$$

$$J_1(u) = 0, \quad (65)$$

$$J_0(u) = 2(\varrho^2 - u^2)^{1/2} \quad (66)$$

and via (59) and (61) finally

$$G^0 = \frac{64}{45}\varrho^5, \quad H^0 = -\frac{8}{3}\varrho^4. \quad (67)$$

For  $G_{\alpha_1}^0$  and  $H_{\alpha_1}^0$ , one has to vary  $\alpha_1$  to obtain the bounds  $\bar{u} = \varrho + \alpha_1\varrho^2$ ,  $\bar{v}(u) = \sqrt{\varrho^2 - u^2 + 2\alpha_1 u^3}$ ,  $\underline{v}(u) \doteq -\bar{v}(u)$ . The density  $f(u, v)$  within the so-given bounds is  $1/\det(D\mathbf{u})$  at the location  $(x(u, v), y(u, v))$  with  $x = u - \alpha_1 u^2 + \mathcal{O}(\varrho^3)$ ,  $y = v$ , i.e.  $f(u, v) = 1 - 2\alpha_1 u + \mathcal{O}(\varrho^2)$ . Thus we have

$$J_2(u) \doteq \frac{2}{3}(1 - 2\alpha_1 u)(\varrho^2 - u^2 + 2\alpha_1 u^3)^{3/2}, \quad (68)$$

$$J_1(u) = 0, \quad (69)$$

$$J_0(u) \doteq 2(1 - 2\alpha_1 u)(\varrho^2 - u^2 + 2\alpha_1 u^3)^{1/2} \quad (70)$$

and therefore by (59), (61)

$$G_{\alpha_1}^0 \doteq \frac{d}{d\alpha_1} \int_0^{\bar{u}} \frac{8}{3}(1 - 2\alpha_1 u)^2(\varrho^2 - u^2 + 2\alpha_1 u^3)^2 du \Big|_{\alpha_1=0} = -\frac{8}{9}\varrho^6, \quad (71)$$

$$H_{\alpha_1}^0 \doteq -\frac{d}{d\alpha_1} \frac{8}{3} \varrho^4 \Big|_{\alpha_1=0} = 0. \quad (72)$$

Proceeding analogously for the other coefficients, we find the values of  $\bar{u}$ ,  $\bar{v}$ ,  $\underline{v}$  and  $f(u, v)$  and the resulting coefficients compiled in Table 6.

Inserting the values from Table 6 into (62) and (63), we have

$$F(0, 0, 0) = \frac{64}{45} \varrho^5 + \frac{8}{9} \varrho^6 (-\alpha_1 + 2\delta_1 + \beta_2), \quad (73)$$

$$F_{u^*}(0, 0, 0) = \frac{8}{3} \varrho^4, \quad (74)$$

and by orthogonal transform in the  $u$ - $v$  plane

$$\begin{aligned} F(0, 0, \varphi) = & \frac{64}{45} \varrho^5 + \frac{8}{9} \varrho^6 \Big( -(\alpha_1 \cos \varphi + \alpha_2 \sin \varphi) \cos^2 \varphi \\ & - (\beta_1 \cos \varphi + \beta_2 \sin \varphi) \cos \varphi \sin \varphi - (\delta_1 \cos \varphi + \delta_2 \sin \varphi) \sin^2 \varphi \\ & + 2(\alpha_1 \cos \varphi + \alpha_2 \sin \varphi) \sin^2 \varphi - 2(\beta_1 \cos \varphi + \beta_2 \sin \varphi) \cos \varphi \sin \varphi \\ & + 2(\delta_1 \cos \varphi + \delta_2 \sin \varphi) \cos^2 \varphi - 2(-\alpha_1 \sin \varphi + \alpha_2 \cos \varphi) \cos \varphi \sin \varphi \\ & + (-\beta_1 \sin \varphi + \beta_2 \cos \varphi) (\cos^2 \varphi - \sin^2 \varphi) \\ & + 2(-\delta_1 \sin \varphi + \delta_2 \cos \varphi) \cos \varphi \sin \varphi \Big), \end{aligned} \quad (75)$$

$$F_{u^*}(0, 0, \varphi) = \frac{8}{3} \varrho^4 \cos \varphi, \quad (76)$$

$$F_{v^*}(0, 0, \varphi) = \frac{8}{3} \varrho^4 \sin \varphi. \quad (77)$$

Integration (53) then yields

$$\Phi(0, 0) = \frac{\pi}{18} \varrho^6 \begin{pmatrix} \alpha_1 + 3\delta_1 - \beta_2 \\ 3\alpha_2 - \delta_2 - \beta_1 \end{pmatrix}, \quad (78)$$

$$D\Phi(0, 0) = -\frac{2}{3} \pi \varrho^4 \begin{pmatrix} 1 & 0 \\ 0 & 1 \end{pmatrix} \quad (79)$$

and via (54) eventually

$$\begin{pmatrix} u^* \\ v^* \end{pmatrix} = \frac{\varrho^2}{12} \begin{pmatrix} \alpha_1 + 3\delta_1 - \beta_2 \\ 3\alpha_2 + \delta_2 - \beta_1 \end{pmatrix}. \quad (80)$$

Inserting (51), (52) into (80), we see that for  $D\mathbf{u} = \text{diag}(1, 1)$  the Oja median filtering step approximates an explicit time step of size  $\tau = \varrho^2/24$  of the PDE system (22)–(23).  $\square$

Table 6: Integration bounds, densities, integrals  $J_k(u)$  and resulting coefficients  $G_\omega^0$ ,  $H_\omega^0$  of the expansions (62), (63) for  $\omega \in \{\alpha_1, \beta_1, \delta_1, \alpha_2, \beta_2, \delta_2\}$ .  $J_1(u)$  and  $H_\omega^0$  are always zero and therefore omitted. All values are approximated up to higher order terms.

$\omega$	$\bar{u}$	$\bar{v}(u), \underline{v}(u)$	$f(u, v)$	$J_2(u)$	$J_0(u)$	$G_\omega^0$
$\alpha_1$	$\varrho + \alpha_1 \varrho^2$	$\pm \sqrt{\varrho^2 - u^2 + 2\alpha_1 u^3}$	$1 - 2\alpha_1 u$	$\frac{2}{3}(1 - 2\alpha_1 u) \bar{v}(u)^3$	$2(1 - 2\alpha_1 u) \bar{v}(u)$	$-\frac{8}{9} \varrho^6$
$\beta_1$	$\varrho$	$\pm \sqrt{\varrho^2 - u^2 + \beta_1^2 u^4 + \beta_1 u^2}$	$1 - \beta_1 v$	$\frac{2}{3}(\varrho^2 - u^2 + \beta_1^2 u^4)^{3/2}$	$2(\varrho^2 - u^2 + \beta_1^2 u^4)^{1/2}$	0
$\delta_1$	$\varrho$	$\pm \sqrt{(\varrho^2 - u^2)(1 + 2\delta_1 u)}$	1	$\frac{2}{3} \bar{v}(u)^3$	$2 \bar{v}(u)$	$\frac{16}{9} \varrho^6$
$\alpha_2$	$\varrho$	$\pm \sqrt{\varrho^2 - u^2 + \alpha_2 u^4 + \alpha_2 u^2}$	1	$\frac{2}{3}(\varrho^2 - u^2 + \alpha_2^2 u^4)^{3/2}$	$2(\varrho^2 - u^2 + \alpha_2^2 u^4)^{1/2}$	0
$\beta_2$	$\varrho$	$\pm \sqrt{(\varrho^2 - u^2)(1 + 2\beta_2 u)}$	$1 - \beta_2 u$	$\frac{2}{3}(1 - \beta_2 u) \bar{v}^3$	$2(1 - \beta_2 u) \bar{v}$	$\frac{8}{9} \varrho^6$
$\delta_2$	$\varrho$	$\pm \sqrt{\varrho^2 - u^2 + \delta_2(\varrho^2 - u^2)}$	$1 - 2\delta_2 v$	$\frac{2}{3}(\varrho^2 - u^2)^{3/2}$	$2(\varrho^2 - u^2)^{1/2}$	0

## B Second Proof of Lemma 2

As in the previous proof, we express the minimisation condition as  $\Phi(u^*, v^*) = 0$  where  $\Phi(u^*, v^*)$  expresses an anti-gradient of the objective function of the Oja median (the sum of triangle areas) at the median candidate point  $M = (u^*, v^*)$ .

Let  $M = (u^*, v^*)$  with  $u^*, v^* = \mathcal{O}(\varrho^2)$ . For two points  $A = (u_1, v_1)$ ,  $B = (u_2, v_2)$  in the  $u$ - $v$  plane, the force exercised on  $M$  by the negative gradient of the area of triangle  $MAB$  is  $\frac{1}{2}F_{M;AB}$  where

$$F_{M;AB} = \begin{pmatrix} v_2 - v_1 \\ u_1 - u_2 \end{pmatrix} = \begin{pmatrix} v_2 \\ -u_2 \end{pmatrix} - \begin{pmatrix} v_1 \\ -u_1 \end{pmatrix} + \mathcal{O}(\varrho^2) \quad (81)$$

provided the triangle  $MAB$  is positively oriented. If  $MAB$  is negatively oriented, the sign of  $F_{M;AB}$  changes.

Let now  $A$  and  $B$  given by

$$A = (u(x_1, y_1), v(x_1, y_1)) , \quad (82)$$

$$B = (u(x_2, y_2), v(x_2, y_2)) \quad (83)$$

with  $(x_1, y_1), (x_2, y_2) \in D_\varrho(\mathbf{0})$ .

Aggregating the forces  $F_{M;AB}$  directly by integration over  $x_1, y_1, x_2, y_2$ , and denoting again by  $\doteq$  equality up to higher order terms, one sees that the resulting force can be stated as

$$\begin{aligned} \Phi &:= \frac{1}{2} \iint_{D_\varrho} \iint_{D_\varrho} F_{M;AB} \, dx_2 \, dy_2 \, dx_1 \, dy_1 \\ &\doteq \frac{1}{2} \iint_{D_\varrho} \iint_{\mathcal{A}_+(x_1, y_1)} \begin{pmatrix} v_2 - v_1 \\ u_1 - u_2 \end{pmatrix} \, dx_2 \, dy_2 \, dx_1 \, dy_1 \\ &\quad - \frac{1}{2} \iint_{D_\varrho} \iint_{\mathcal{A}_-(x_1, y_1)} \begin{pmatrix} v_2 - v_1 \\ u_1 - u_2 \end{pmatrix} \, dx_2 \, dy_2 \, dx_1 \, dy_1 \\ &= \frac{1}{2} \iint_{D_\varrho} \iint_{\mathcal{A}_+(x_1, y_1)} \begin{pmatrix} v_2 \\ -u_2 \end{pmatrix} \, dx_2 \, dy_2 \, dx_1 \, dy_1 \\ &\quad - \frac{1}{2} \iint_{D_\varrho} \iint_{\mathcal{A}_+(x_1, y_1)} \begin{pmatrix} v_1 \\ -u_1 \end{pmatrix} \, dx_2 \, dy_2 \, dx_1 \, dy_1 \\ &\quad - \frac{1}{2} \iint_{D_\varrho} \iint_{\mathcal{A}_-(x_1, y_1)} \begin{pmatrix} v_2 \\ -u_2 \end{pmatrix} \, dx_2 \, dy_2 \, dx_1 \, dy_1 \\ &\quad + \frac{1}{2} \iint_{D_\varrho} \iint_{\mathcal{A}_-(x_1, y_1)} \begin{pmatrix} v_1 \\ -u_1 \end{pmatrix} \, dx_2 \, dy_2 \, dx_1 \, dy_1 . \end{aligned} \quad (84)$$

Here,  $\mathcal{A}_\pm(x_1, y_1)$  denote the regions for  $(x_2, y_2) \in D_\varrho$  for which  $MAB$  is positively or negatively oriented, respectively. Since  $B \in \mathcal{A}_+(x_1, y_1)$  if and only if  $A \in \mathcal{A}_-(x_2, y_2)$  and vice versa, we can switch the roles of  $(x_1, y_1)$  and  $(x_2, y_2)$  in two of the integrals to combine the

previous expressions into

$$\begin{aligned}
\Phi &\doteq - \iint_{D_\varrho} \iint_{\mathcal{A}_+(x_1, y_1)} \begin{pmatrix} v_1 \\ -u_1 \end{pmatrix} dx_2 dy_2 dx_1 dy_1 \\
&\quad + \iint_{D_\varrho} \iint_{\mathcal{A}_-(x_1, y_1)} \begin{pmatrix} v_1 \\ -u_1 \end{pmatrix} dx_2 dy_2 dx_1 dy_1 \\
&= - \iint_{D_\varrho} \begin{pmatrix} v_1 \\ -u_1 \end{pmatrix} (|\mathcal{A}_+(x_1, y_1)| - |\mathcal{A}_-(x_1, y_1)|) dx_1 dy_1
\end{aligned} \tag{85}$$

where  $|\mathcal{A}_\pm(x_1, y_1)|$  denote the areas of the respective regions.

It remains to determine the area differences

$$\Delta\mathcal{A}(x_1, y_1) := |\mathcal{A}_+(x_1, y_1)| - |\mathcal{A}_-(x_1, y_1)| \tag{86}$$

for all  $(x_1, y_1) \in D_\varrho$ .

To this end, we use again the Taylor expansion (50). For  $u^* = v^* = 0$  and  $\alpha_1 = \beta_1 = \delta_1 = \alpha_2 = \beta_2 = \delta_2 = 0$  we have  $u(x, y) = x$ ,  $v(x, y) = y$ , and  $\mathcal{A}_+(x_1, y_1)$  and  $\mathcal{A}_-(x_1, y_1)$  are half-discs separated by the diameter of  $D_\varrho$  through  $M$  and  $A$ . Generally, the two regions are separated by the curve  $(u_1 - u^*)(v_2 - v^*) - (u_2 - u^*)(v_1 - v^*) = 0$ , which after inserting (50) and dropping higher order terms becomes

$$\begin{aligned}
0 &= x_1 y_2 - x_2 y_1 - u^*(y_2 - y_1) - v^*(x_1 - x_2) \\
&\quad + \alpha_1(x_1^2 y_2 - x_2^2 y_1) + \beta_1(x_1 y_1 y_2 - x_2 y_1 y_2) + \delta_1(y_1^2 y_2 - y_1 y_2^2) \\
&\quad + \alpha_2(x_1 x_2^2 - x_1^2 x_2) + \beta_2(x_1 x_2 y_2 - x_1 x_2 y_1) + \delta_2(x_1 y_2^2 - x_2 y_1^2) .
\end{aligned} \tag{87}$$

To determine the deviation of this line from the bisecting diameter mentioned above, we introduce coordinates aligned to the line  $MA$  by  $x_1 = r \cos \varphi$ ,  $y_1 = r \sin \varphi$  and  $x_2 = s \cos \varphi - t \sin \varphi$ ,  $y_2 = s \sin \varphi + t \cos \varphi$ . We can then write (87) up to higher order terms as

$$\begin{aligned}
t = t(s) &\doteq s^2(\alpha_1 \cos^2 \varphi \sin \varphi + \beta_1 \cos \varphi \sin^2 \varphi + \delta_1 \sin^3 \varphi \\
&\quad - \alpha_2 \cos^3 \varphi - \beta_2 \cos^2 \varphi \sin \varphi - \delta_2 \cos \varphi \sin^2 \varphi) \\
&\quad + s \left( \frac{u^*}{r} \sin \varphi - \frac{v^*}{r} \cos \varphi \right. \\
&\quad \quad - r\alpha_1 \cos^2 \varphi \sin \varphi - r\beta_1 \cos \varphi \sin^2 \varphi - r\delta_1 \sin^3 \varphi \\
&\quad \quad \left. + r\alpha_2 \cos^3 \varphi + r\beta_2 \cos^2 \varphi \sin \varphi + r\delta_2 \cos \varphi \sin^2 \varphi \right) \\
&\quad - \frac{u^*}{r} \sin \varphi + \frac{v^*}{r} \cos \varphi .
\end{aligned} \tag{88}$$

Up to higher order terms, the area difference  $\Delta\mathcal{A}(x_1, y_1)$  is minus double the area between this line and the  $s$ -axis in the interval  $s \in [-\varrho, \varrho]$ , i.e.

$$\begin{aligned}
\Delta\mathcal{A}(x_1, y_1) &\doteq -2 \int_{-\varrho}^{\varrho} t(s) ds \\
&\doteq 4\varrho(u^* \sin \varphi - v^* \cos \varphi) \\
&\quad - \frac{4}{3} \varrho^3 (\alpha_1 \cos^2 \varphi \sin \varphi + \beta_1 \cos \varphi \sin^2 \varphi + \delta_1 \sin^3 \varphi \\
&\quad \quad - \alpha_2 \cos^3 \varphi - \beta_2 \cos^2 \varphi \sin \varphi - \delta_2 \cos \varphi \sin^2 \varphi) .
\end{aligned} \tag{89}$$

Inserting (50), (86) and (89) into (85) yields

$$\begin{aligned}
\Phi &\doteq - \iint_{D_\varrho} \begin{pmatrix} -y - \alpha_2 x^2 - \beta_2 xy - \delta^2 y^2 \\ x + \alpha_1 x^2 + \beta_1 xy + \delta_1 y^2 \end{pmatrix} \Delta \mathcal{A}(x, y) \, dx \, dy \\
&\doteq \frac{1}{2} \int_0^\varrho \int_0^{2\pi} r^2 \begin{pmatrix} \sin \varphi \\ -\cos \varphi \end{pmatrix} \Delta \mathcal{A}(x, y) \, d\varphi \, dr \\
&= \int_0^\varrho r^2 \, dr \left( 2\varrho \left( u^* \int_0^{2\pi} \begin{pmatrix} \sin^2 \varphi \\ -\cos \varphi \sin \varphi \end{pmatrix} \, d\varphi - v^* \int_0^{2\pi} \begin{pmatrix} \cos \varphi \sin \varphi \\ -\cos^2 \varphi \end{pmatrix} \, d\varphi \right) \right. \\
&\quad - \frac{2}{3} \varrho^3 \left( \alpha_1 \int_0^{2\pi} \begin{pmatrix} \cos^2 \varphi \sin^2 \varphi \\ -\cos^3 \varphi \sin \varphi \end{pmatrix} \, d\varphi + \beta_1 \int_0^{2\pi} \begin{pmatrix} \cos \varphi \sin^3 \varphi \\ -\cos^2 \varphi \sin^2 \varphi \end{pmatrix} \, d\varphi \right. \\
&\quad + \delta_1 \int_0^{2\pi} \begin{pmatrix} \sin^4 \varphi \\ -\cos \varphi \sin^3 \varphi \end{pmatrix} \, d\varphi - \alpha_2 \int_0^{2\pi} \begin{pmatrix} \cos^3 \varphi \sin \varphi \\ -\cos^4 \varphi \end{pmatrix} \, d\varphi \\
&\quad \left. \left. - \beta_2 \int_0^{2\pi} \begin{pmatrix} \cos^2 \varphi \sin^2 \varphi \\ -\cos^3 \varphi \sin \varphi \end{pmatrix} \, d\varphi - \delta_2 \int_0^{2\pi} \begin{pmatrix} \cos \varphi \sin^3 \varphi \\ -\cos^2 \varphi \sin^2 \varphi \end{pmatrix} \, d\varphi \right) \right) \\
&= \frac{2}{3} \pi \varrho^4 \begin{pmatrix} u^* \\ v^* \end{pmatrix} - \frac{1}{18} \pi \varrho^6 \begin{pmatrix} \alpha_1 + 3\delta_1 - \beta_2 \\ 3\alpha_2 + \delta_2 - \beta_1 \end{pmatrix}, \tag{90}
\end{aligned}$$

which reproduces the result (78), (79) from the first proof such that one can again infer (80) and thereby (22), (23).  $\square$

## C Proof of Lemma 3

We start with the Taylor expansion of  $\mathbf{u}(x, y, z)$  around  $(0, 0, 0)$  up to second order given as

$$u(x, y, z) = x + \alpha_1 x^2 + \beta_1 xy + \gamma_1 xz + \delta_1 y^2 + \varepsilon_1 yz + \zeta_1 z^2, \tag{91}$$

$$v(x, y, z) = y + \alpha_2 x^2 + \beta_2 xy + \gamma_2 xz + \delta_2 y^2 + \varepsilon_2 yz + \zeta_2 z^2, \tag{92}$$

$$w(x, y, z) = z + \alpha_3 x^2 + \beta_3 xy + \gamma_3 xz + \delta_3 y^2 + \varepsilon_3 yz + \zeta_3 z^2 \tag{93}$$

where  $\alpha_1 = \frac{1}{2}u_{xx}$ ,  $\beta_1 = u_{xy}$  etc.

Similarly as in Appendix A for the bivariate planar case, we seek the point  $M := (u^*, v^*, w^*)$  that minimises the integral over all volumes of tetrahedra  $MABC$  with  $A = (u_1, v_1, w_1)$ ,  $B = (u_2, v_2, w_2)$ ,  $C = (u_3, v_3, w_3)$  where  $(u_i, v_i, w_i) = (u(x_i, y_i, z_i), v(x_i, y_i, z_i), w(x_i, y_i, z_i))$  with  $(x_i, y_i, z_i) \in B_\varrho(0, 0, 0)$ , weighted with the density  $f(u_1, v_1, w_1)f(u_2, v_2, w_2)f(u_3, v_3, w_3)$ .

For each tetrahedron  $MABC$ , the negative gradient of its volume as a function of  $M$  is a force vector  $\frac{1}{6}F_{M;ABC}$  perpendicular to the plane  $ABC$  with a length proportional to the area  $|ABC|$  of the triangle  $ABC$ . Assuming positive orientation of that triangle,  $F_{M;ABC}$  equals the vector (cross) product  $-(u_2 - u_1, v_2 - v_1, w_2 - w_1) \times (u_3 - u_1, v_3 - v_1, w_3 - w_1)$ .

Organising the integration over point triples  $(A, B, C)$  again by orientations of the force vectors, we consider the resultant  $F(u^*, v^*, w^*, \mathbf{p})$  of all forces in direction of any given unit vector  $\mathbf{p} \in \mathbb{S}^2$ . Linearising for  $(u^*, v^*, w^*)$  around  $\mathbf{0}$ ,

$$\begin{pmatrix} u^* \\ v^* \\ w^* \end{pmatrix} = -(\mathbf{D}\Phi(0, 0, 0))^{-1} \Phi(0, 0, 0) \tag{94}$$

(compare (54)), and considering first the case where  $\mathbf{p} = \mathbf{e}_1 = (1, 0, 0)$  is the first coordinate vector, we can state the analogue of (55) as

$$F(0, 0, 0, \mathbf{e}_1) = \int_0^{+\infty} \int_{-\infty}^{+\infty} \int_{-\infty}^{+\infty} \int_{-\infty}^{+\infty} \int_{-\infty}^{+\infty} \int_{-\infty}^{+\infty} \int_{-\infty}^{+\infty} f(u, v_1, w_1) f(u, v_2, w_2) f(u, v_3, w_3) \\ \times ((v_2 - v_1)(w_3 - w_1) - (v_3 - v_1)(w_2 - w_1))^2 \\ dw_3 dv_3 dw_2 dv_2 dw_1 dv_1 du . \quad (95)$$

The appearance of the square of the area  $(v_2 - v_1)(w_3 - w_1) - (v_3 - v_1)(w_2 - w_1)$  is again due to the Radon-like polar coordinates underlying the integration over directions.

As in Appendix A, the indefinite integrals can be limited to finite intervals  $u \in [0, \bar{u}]$ ,  $v_i \in [\underline{v}(u), \bar{v}(u)]$ ,  $w_i \in [\underline{w}(u, v_i), \bar{w}(u, v_i)]$  for  $i = 1, 2, 3$ . Expanding

$$((v_2 - v_1)(w_3 - w_1) - (v_3 - v_1)(w_2 - w_1))^2 \\ = \sum_{\substack{i,j \in \{1,2,3\} \\ i \neq j}} v_i^2 w_j^2 - 2 \sum_{\substack{i,j \in \{1,2,3\} \\ i < j}} v_i w_i v_j w_j - 2 \sum_{\substack{i,j,k \in \{1,2,3\} \\ i < j; k \neq i,j}} v_i v_j w_k^2 \\ - 2 \sum_{\substack{i,j,k \in \{1,2,3\} \\ j < k; i \neq j,k}} v_i^2 w_j w_k + 2 \sum_{\substack{i,j,k \in \{1,2,3\} \\ i \neq j \neq k \neq i}} v_i w_j v_k w_k \quad (96)$$

then leads to

$$F(0, 0, 0, \mathbf{e}_1) = \int_0^{\bar{u}} (6J_{20}(u)J_{02}(u)J_{00}(u) - 6J_{11}(u)^2 J_{00}(u) - 6J_{02}(u)J_{10}(u)^2 \\ - 6J_{20}(u)J_{01}(u)^2 + 12J_{10}(u)J_{01}(u)J_{00}(u)) du \quad (97)$$

with

$$J_{kl}(u) := \int_{\underline{v}(u)}^{\bar{v}(u)} \int_{\underline{w}(u,v)}^{\bar{w}(u,v)} f(u, v, w) v^k w^l dw dv \quad (98)$$

for  $k, l = 0, 1, 2$ .

We linearise  $F(0, 0, 0, \mathbf{e}_1)$  with regard to the 18 coefficients  $\omega \in \{\alpha_i, \beta_i, \gamma_i, \delta_i, \varepsilon_i, \zeta_i \mid i = 1, 2, 3\}$  of the Taylor expansion (91)–(93)

$$F(0, 0, 0, \mathbf{e}_1) = G^0 + \sum_{\omega} G_{\omega}^0 \omega . \quad (99)$$

Like in the bivariate case of Appendix A, cross-effects between the coefficients  $\omega$  take effect only in higher-order terms that can be neglected for our purpose. Moreover,  $G^0$  is again a constant that vanishes in the integration over directions, so we refrain from explicitly calculating it.

To calculate the value  $G_{\omega}^0$  for each coefficient  $\omega$  one can then assume that only this particular coefficient varies around 0 while all other coefficients vanish. For 10 of the coefficients  $\omega$  one calculates then the integration bounds  $\bar{u}$ ,  $\underline{v}(u)$ ,  $\bar{v}(u)$ ,  $\underline{w}(u, v)$ ,  $\bar{w}(u, v)$  and the density function  $f(u, v, w)$  as stated in Table 7, the respective integrals  $J_{kl}(u)$  as given in Table 8 and finally using (97) the coefficients  $G_{\omega}^0$  which are again listed in Table 7. The remaining 8 coefficients need not be calculated in this tedious way as they can be derived from the

obvious symmetry of  $F(0, 0, 0, \mathbf{e}_1)$  under the exchange of  $y$  and  $z$ ; the detailed symmetries of coefficients are also stated in Table 7.

For the derivatives of  $F$  we have

$$F_{u^*}(0, 0, 0, \mathbf{e}_1) = H^0(1 + \mathcal{O}(\varrho^2)) , \quad (100)$$

$$F_{v^*}(0, 0, 0, \mathbf{e}_1) = 0 , \quad (101)$$

$$F_{w^*}(0, 0, 0, \mathbf{e}_1) = 0 . \quad (102)$$

Here,  $H^0$  is calculated from the unperturbed case  $u = x, v = y, w = z$  via

$$J_{20}(0) = J_{02}(0) = \frac{1}{4}\pi\varrho^4 , \quad (103)$$

Table 7: Integration bounds, densities and resulting coefficients  $G_\omega^0$  of the expansion (99) for  $\omega \in \{\alpha_i, \beta_i, \gamma_i, \delta_i, \varepsilon_i, \zeta_i \mid i = 1, 2, 3\}$ . Coefficients  $H_\omega^0$  are always zero and therefore omitted. All values are approximated up to higher order terms. The integrals  $J_{kl}(u)$  are found in Table 8. Coefficients listed in the second column are inferred from the ones in the first column by symmetry.

$\omega$	$\omega$ (symm.)	$\bar{u}$	$\bar{v}(u), v(u)$	$\bar{w}(u, v), w(u, v)$	$f(u, v, w)$	$G_\omega^0$
$\alpha_1$		$\varrho + \alpha_1 \varrho^2$	$\pm \sqrt{\varrho^2 - u^2 + 2\alpha_1 u^3}$	$\pm \sqrt{\varrho^2 - u^2 + 2\alpha_1 u^3 - v^2}$	$1 - 2\alpha_1 u$	$-\frac{1}{8}\pi^3 \varrho^{12}$
$\gamma_1$	$\beta_1$	$\varrho$	$\pm \sqrt{\varrho^2 - u^2}$	$\pm \sqrt{\varrho^2 - u^2 - v^2 + \gamma_1 u^2}$	$1 - \gamma_1 w$	0
$\delta_1$	$\zeta_1$	$\varrho$	$\pm \sqrt{(\varrho^2 - u^2)(1 + 2\delta_1 u)}$	$\pm \sqrt{\varrho^2 - u^2 + 2\delta_1 u v^2 - v^2}$	1	$\frac{5}{32}\pi^3 \varrho^{12}$
$\varepsilon_1$		$\varrho$	$\pm \sqrt{\varrho^2 - u^2}$	$\pm \sqrt{\varrho^2 - u^2 - v^2 + \varepsilon_1 u v}$	1	0
$\beta_2$	$\gamma_3$	$\varrho$	$\pm \sqrt{(\varrho^2 - u^2)(1 + 2\beta_2 u)}$	$\pm \sqrt{\varrho^2 - u^2 + 2\beta_2 u v^2 - v^2}$	$1 - \beta_2 u$	$\frac{1}{16}\pi^3 \varrho^{12}$
$\gamma_2$	$\beta_3$	$\varrho$	$\pm \sqrt{\varrho^2 - u^2}$	$\pm \sqrt{\varrho^2 - u^2 - v^2 + \gamma_2 u v}$	1	0
$\delta_2$	$\zeta_3$	$\varrho$	$\pm \sqrt{\varrho^2 - u^2 + \delta_2(\varrho^2 - u^2)}$	$\pm \sqrt{\varrho^2 - u^2 - v^2 + 2\delta_2 v^3}$	$1 - 2\delta_2 v$	0
$\varepsilon_2$	$\varepsilon_3$	$\varrho$	$\pm \sqrt{\varrho^2 - u^2}$	$\pm \sqrt{\varrho^2 - u^2 - v^2 + \varepsilon_2 v^2}$	$1 - \varepsilon_2 w$	0
$\zeta_2$	$\delta_3$	$\varrho$	$\pm \sqrt{\varrho^2 - u^2}$	$\pm \sqrt{\varrho^2 - u^2 - v^2(1 + \zeta_2 v)}$	1	0
$\alpha_3$	$\alpha_2$	$\varrho$	$\pm \sqrt{\varrho^2 - u^2}$	$\pm \sqrt{\varrho^2 - u^2 - v^2 + \alpha_3 u^2}$	1	0

Table 8: Integrals  $J_{kl}(u)$  from the computation of the coefficients  $G_\omega^0$  from Table 7. All values are approximated up to higher order terms. For abbreviation,  $U := \varrho^2 - u^2$  is used.

$\omega$	$J_{20}(u)$	$J_{11}(u)$	$J_{02}(u)$	$J_{10}(u)$	$J_{01}(u)$	$J_{00}(u)$
$\alpha_1$	$\frac{1}{4}\pi(1 - 2\alpha_1 u)\bar{v}^4$	0	$\frac{1}{4}\pi(1 - 2\alpha_1 u)\bar{v}^4$	0	0	$\pi(1 - 2\alpha_1 u)\bar{v}^2$
$\gamma_1$	$\frac{1}{4}\pi U^2$	0	$\frac{1}{4}\pi U^2$	0	$-\frac{1}{4}\pi\gamma_1 U(\varrho^2 - 5u^2)$	$\pi U$
$\delta_1$	$\frac{1}{4}\pi(1 + \delta_1 u)^3 U^2$	0	$\frac{1}{4}\pi(1 + \delta_1 u)U^2$	0	0	$\pi(1 + \delta_1 u)U$
$\varepsilon_1$	$\frac{1}{4}\pi U^2$	$\frac{1}{2}\pi\varepsilon_1 u U^2$	$\frac{1}{4}\pi U^2$	0	0	$\pi U$
$\beta_2$	$\frac{1}{4}\pi(1 + \beta_2 u)^2 U^2$	0	$\frac{1}{4}\pi U^2$	0	0	$\pi U$
$\gamma_2$	$\frac{1}{4}\pi U^2$	$\frac{1}{2}\pi\gamma_2 u U^2$	$\frac{1}{4}\pi U^2$	0	0	$\pi U$
$\delta_2$	$\frac{1}{4}\pi U^2$	0	$\frac{1}{4}\pi U^2$	$\frac{1}{4}\pi\delta_2 U^2$	0	$\pi U$
$\varepsilon_2$	$\frac{1}{4}\pi U^2$	0	$\frac{1}{4}\pi U^2$	0	0	$\pi U$
$\zeta_2$	$\frac{1}{4}\pi U^2$	0	$\frac{1}{4}\pi U^2$	$\frac{1}{4}\pi\zeta_2 U^2$	0	$\pi U$
$\alpha_3$	$\frac{1}{4}\pi U^2$	0	$\frac{1}{4}\pi U^2$	0	$\pi\alpha_3 u^2 U$	$\pi U$

$$J_{00}(0) = \pi \varrho^2, \quad (104)$$

$$J_{11}(0) = J_{10}(0) = J_{01}(0) = 0. \quad (105)$$

Thus only the first summand of the integrand of (97) is non-zero, leading to

$$H^0 = -6J_{20}(0)J_{02}(0)J_{00}(0) = -\frac{3}{8}\pi^3\varrho^{10}. \quad (106)$$

From the so obtained expressions

$$F(0, 0, 0, \mathbf{e}_1) \doteq G^0 + \frac{1}{32}\pi^3\varrho^{12}(-4\alpha_1 + 5\delta_1 + 5\zeta_1 + 2\beta_2 + 2\gamma_3), \quad (107)$$

$$F_{u^*}(0, 0, 0, \mathbf{e}_1) \doteq -\frac{3}{8}\pi^3\varrho^{10} \quad (108)$$

general expressions for  $F(0, 0, 0, \mathbf{p})$  and its derivatives w.r.t.  $u^*, v^*, w^*$  can be obtained. Given the parametrisation

$$\mathbf{p} = \mathbf{p}(\varphi, \psi) = (\cos \varphi, \sin \varphi \cos \psi, \sin \varphi \sin \psi)^T \quad (109)$$

one can use e.g. the rotation matrix

$$R = \begin{pmatrix} \cos \varphi & \sin \varphi \cos \psi & \sin \varphi \sin \psi \\ -\sin \varphi & \cos \varphi \cos \psi & \cos \varphi \sin \psi \\ 0 & \sin \psi & -\cos \psi \end{pmatrix} \quad (110)$$

to transform the  $(u, v, w)$  and  $(x, y, z)$  coordinates simultaneously. (There is a degree of freedom in the choice of  $R$  that corresponds to a rotation around the direction of  $\mathbf{p}$ .)

Integration over directions then yields

$$\begin{aligned} \Phi(0, 0, 0) &= \int_{\mathbb{S}^2} F(0, 0, 0, \mathbf{p}) \mathbf{p} \, d\sigma(\mathbf{p}) \\ &= \int_0^\pi \int_0^{2\pi} F(0, 0, 0, \mathbf{p}(\varphi, \psi)) \begin{pmatrix} \cos \varphi \\ \sin \varphi \cos \psi \\ \sin \varphi \sin \psi \end{pmatrix} \sin \varphi \, d\psi \, d\varphi \\ &= \frac{\pi^6}{40} \varrho^{12} \begin{pmatrix} 2\alpha_1 + 4(\delta_1 + \zeta_1) - (\beta_2 + \gamma_3) \\ 2\delta_2 + 4(\alpha_2 + \zeta_2) - (\beta_1 + \varepsilon_3) \\ 2\zeta_3 + 4(\alpha_3 + \delta_3) - (\gamma_1 + \varepsilon_2) \end{pmatrix} \end{aligned} \quad (111)$$

and similarly

$$\mathbf{D}\Phi(0, 0, 0) = -\frac{\pi^4}{2} \varrho^{10} \begin{pmatrix} 1 & 0 & 0 \\ 0 & 1 & 0 \\ 0 & 0 & 1 \end{pmatrix} \quad (112)$$

and by (94)

$$\begin{pmatrix} u^* \\ v^* \\ w^* \end{pmatrix} = \frac{\varrho^2}{20} \begin{pmatrix} 2\alpha_1 + 4(\delta_1 + \zeta_1) - (\beta_2 + \gamma_3) \\ 2\delta_2 + 4(\alpha_2 + \zeta_2) - (\beta_1 + \varepsilon_3) \\ 2\zeta_3 + 4(\alpha_3 + \delta_3) - (\gamma_1 + \varepsilon_2) \end{pmatrix}, \quad (113)$$

hence an explicit time step of size  $\tau = \varrho^2/20$  of the PDE system (35)–(37).  $\square$

## D Proof of Lemma 4

We start again from the Taylor expansion (91)–(93) of the function  $\mathbf{u}$  around the point  $\mathbf{x} = \mathbf{0}$ .

The  $L^1$  median  $(\mathbf{u}^*, \mathbf{v}^*, \mathbf{w}^*)$  of the function values of  $\mathbf{u}$  within the structuring element  $B_\varrho$  is determined by the equilibrium conditions

$$0 = \iiint_{B_\varrho} \frac{\mathbf{u}(x, y, z) - \mathbf{u}^*}{|\mathbf{u}(x, y, z) - \mathbf{u}^*|} dz dy dx . \quad (114)$$

With the goal of the PDE approximation, we will determine the median as linear function of the Taylor coefficients. Cross-effects between the Taylor coefficients will again be restricted to higher order terms in  $\varrho$  that can be neglected in our asymptotic analysis for  $\varrho \rightarrow 0$ . We can therefore study the effects of the Taylor coefficients separately.

To start with  $\alpha_1$ , we insert in (114) the function  $u = x + \alpha_1 x^2$ ,  $v = y$ ,  $w = z$ , and obtain the three conditions

$$0 = \iiint_{B_\varrho} \frac{x + \alpha_1 x^2 - u^*}{\sqrt{N(x, y, z)}} dz dy dx , \quad (115)$$

$$0 = \iiint_{B_\varrho} \frac{y - v^*}{\sqrt{N(x, y, z)}} dz dy dx , \quad (116)$$

$$0 = \iiint_{B_\varrho} \frac{z - w^*}{\sqrt{N(x, y, z)}} dz dy dx , \quad (117)$$

where

$$N(x, y, z) = (x + \alpha_1 x^2 - u^*)^2 + (y - v^*)^2 + (z - w^*)^2 . \quad (118)$$

Condition (116) can be turned by substituting  $-y$  for  $y$  into the same equation with  $-v^*$  in place of  $v^*$ , i.e. for any triple  $(u^*, v^*, w^*)$  that satisfies the three conditions,  $(u^*, -v^*, w^*)$  does the same. By the convexity of the objective function of the  $L^1$  median it follows that  $(u^*, 0, w^*)$  is in this case also a minimiser. The same argument works for  $w^*$ . Hence, we can seek the median as  $(u^*, v^*, w^*) = (\lambda \varrho^2, 0, 0)$  and need to consider only Condition (115). Using the substitution  $x = \xi \varrho$ ,  $y = \eta \varrho$ ,  $z = \zeta \varrho$  we obtain

$$0 = \iiint_{B_1} \frac{\xi + (\alpha_1 \xi^2 - \lambda) \varrho}{\sqrt{(\xi + (\alpha_1 \xi^2 - \lambda) \varrho)^2 + \eta^2 + \zeta^2}} d\zeta d\eta d\xi . \quad (119)$$

Splitting this integral into the integrals over  $B_{\varrho^{2/5}}$  and  $B_1 \setminus B_{\varrho^{2/5}}$ , we see that the integral over  $B_{\varrho^{2/5}}$  is of order  $\mathcal{O}(\varrho^{6/5})$  because the integrand is absolutely bounded by 1. In the domain of the second integral, we have that  $(\alpha_1 \xi^2 - \lambda) \varrho / (\xi^2 + \eta^2 + \zeta^2) = \mathcal{O}(\varrho^{3/5})$  and therefore by Taylor expansion

$$\begin{aligned} & ((\xi + (\alpha_1 \xi^2 - \lambda) \varrho)^2 + \eta^2 + \zeta^2)^{-1/2} \\ &= (\xi^2 + \eta^2 + \zeta^2)^{-1/2} \left( 1 - \frac{(\alpha_1 \xi^2 - \lambda) \varrho}{\xi^2 + \eta^2 + \zeta^2} + \mathcal{O}(\varrho^{6/5}) \right) \end{aligned} \quad (120)$$

which leads to

$$0 = \underbrace{\iiint_{B_1 \setminus B_{\varrho^{2/5}}} \frac{\xi}{\sqrt{\xi^2 + \eta^2 + \zeta^2}} d\zeta d\eta d\xi}_{=0} + \varrho \iiint_{B_1 \setminus B_{\varrho^{2/5}}} \frac{\alpha_1 \xi^2 - \lambda}{\sqrt{\xi^2 + \eta^2 + \zeta^2}} d\zeta d\eta d\xi$$

$$\begin{aligned}
& -\varrho \iiint_{B_1 \setminus B_{\varrho^{2/5}}} \frac{\alpha_1 \xi^2 - \lambda}{(\xi^2 + \eta^2 + \zeta^2)^{3/2}} d\zeta d\eta d\xi + \mathcal{O}(\varrho^{6/5}) \\
& = \varrho \iiint_{B_1 \setminus B_{\varrho^{2/5}}} \frac{(\alpha_1 \xi^2 - \lambda)(\xi^2 + \eta^2 + \zeta^2 - \xi^2)}{(\xi^2 + \eta^2 + \zeta^2)^{3/2}} d\zeta d\eta d\xi + \mathcal{O}(\varrho^{6/5})
\end{aligned} \tag{121}$$

and finally, by neglecting  $\mathcal{O}(\varrho^{1/5})$  terms, to

$$\begin{aligned}
\frac{\lambda}{\alpha_1} &= \frac{\iiint_{B_1 \setminus B_{\varrho^{2/5}}} \xi^2(\eta^2 + \zeta^2)/(\xi^2 + \eta^2 + \zeta^2)^{3/2} d\zeta d\eta d\xi}{\iiint_{B_1 \setminus B_{\varrho^{2/5}}} (\eta^2 + \zeta^2)/(\xi^2 + \eta^2 + \zeta^2)^{3/2} d\zeta d\eta d\xi} \\
&= \frac{(1 - \varrho^{8/5}) \cdot 2\pi/15}{(1 - \varrho^{4/5}) \cdot 4\pi/3} \xrightarrow{\varrho \rightarrow 0} \frac{1}{10},
\end{aligned} \tag{122}$$

thus in the limit  $(u^*, v^*, w^*) = \frac{1}{20}\varrho^2(u_{xx}, 0, 0)$ .

By permutation of variables, one finds  $(u^*, v^*, w^*) = \frac{1}{20}\varrho^2(0, v_{yy}, 0)$  if  $u = x$ ,  $v = y + \delta_2 y^2$ ,  $w = z$ , and  $(u^*, v^*, w^*) = \frac{1}{20}\varrho^2(0, 0, w_{zz})$  if  $u = x$ ,  $v = y$ ,  $w = z + \zeta_3 z^2$ .

Turning to the case  $u = x + \delta_1 y^2$ ,  $v = y$ ,  $w = z$ , we can conclude  $v^* = w^* = 0$  by a similar symmetry argument as before. For the remaining condition

$$0 = \iiint_{B_\varrho} \frac{x + \delta_1 y^2 - u^*}{\sqrt{N(x, y, z)}} dz dy dx, \tag{123}$$

$$N(x, y, z) = (x + \delta_1 y^2 - u^*)^2 + (y - v^*)^2 + (z - w^*)^2, \tag{124}$$

we proceed by the same substitutions, splitting of the integral domain, and Taylor expansion of the denominator to finally obtain

$$\begin{aligned}
\frac{\lambda}{\delta_1} &= \frac{\iiint_{B_1 \setminus B_{\varrho^{2/5}}} \eta^2(\eta^2 + \zeta^2)/(\xi^2 + \eta^2 + \zeta^2)^{3/2} d\zeta d\eta d\xi}{\iiint_{B_1 \setminus B_{\varrho^{2/5}}} (\eta^2 + \zeta^2)/(\xi^2 + \eta^2 + \zeta^2)^{3/2} d\zeta d\eta d\xi} \\
&= \frac{(1 - \varrho^{8/5}) \cdot 4\pi/15}{(1 - \varrho^{4/5}) \cdot 4\pi/3} \xrightarrow{\varrho \rightarrow 0} \frac{1}{5},
\end{aligned} \tag{125}$$

thus in the limit  $(u^*, v^*, w^*) = \frac{1}{20}\varrho^2(2u_{yy}, 0, 0)$ .

By permutation of variables this also determines the  $u_{zz}$ ,  $v_{xx}$ ,  $v_{zz}$ ,  $w_{xx}$  and  $w_{yy}$  contributions of the PDE system (35)–(37).

For  $u = x + \beta xy$ ,  $v = y$ ,  $w = z$  we find  $u^* = w^* = 0$  by symmetry considerations and evaluate the second component of (114) with  $v^* = \mu\varrho^2$  to

$$\begin{aligned}
\frac{\mu}{\beta_1} &= -\frac{\iiint_{B_1 \setminus B_{\varrho^{2/5}}} \xi^2 \eta^2 / (\xi^2 + \eta^2 + \zeta^2)^{3/2} d\zeta d\eta d\xi}{\iiint_{B_1 \setminus B_{\varrho^{2/5}}} (\xi^2 + \zeta^2) / (\xi^2 + \eta^2 + \zeta^2)^{3/2} d\zeta d\eta d\xi} \\
&= -\frac{(1 - \varrho^{8/5}) \cdot \pi/15}{(1 - \varrho^{4/5}) \cdot 4\pi/3} \xrightarrow{\varrho \rightarrow 0} -\frac{1}{20},
\end{aligned} \tag{126}$$

thus in the limit  $(u^*, v^*, w^*) = \frac{1}{20}\varrho^2(0, -u_{xy}, 0)$ .

Permutation of the variables yields all remaining terms of (35)–(37).  $\square$

## E Proof of Lemma 5

The Taylor expansion of  $\mathbf{u}(x, y)$  around  $(0, 0, 0)$  up to second order is given as

$$u(x, y) = x + \alpha_1 x^2 + \beta_1 xy + \delta_1 y^2, \quad (127)$$

$$v(x, y) = y + \alpha_2 x^2 + \beta_2 xy + \delta_2 y^2, \quad (128)$$

$$w(x, y) = \alpha_3 x^2 + \beta_3 xy + \delta_3 y^2, \quad (129)$$

where  $\alpha_1 = \frac{1}{2}u_{xx}$ ,  $\beta_1 = u_{xy}$  etc.

We will again express the median of data values within the structuring element  $D_\varrho$  in terms of the Taylor coefficients, neglecting terms of higher order in  $\varrho$ . As in the settings before, cross-effects between the Taylor coefficients influence only higher-order terms such that the Taylor coefficients can be considered separately.

As long as  $\alpha_3 = \beta_3 = \delta_3 = 0$ , the component  $w$  is identically zero, and thus  $w^* = 0$ . Moreover, the effects of  $\alpha_1, \dots, \delta_2$  on  $u^*$  and  $v^*$  are the same as in Lemma 2, such that we need only to consider  $\alpha_3, \beta_3$  and  $\delta_3$ .

Since by the influence of  $w$  which varies just in order  $\mathcal{O}(\varrho^2)$  around zero, the triangles whose area sum is minimised by the 2D Oja median stay approximately in the  $u$ - $v$  plane and their deformation is restricted to higher order terms, neither of  $\alpha_3, \beta_3$  and  $\delta_3$  influences the first two median components  $u^*, v^*$  asymptotically.

It remains to study  $w^*$ . For the case  $u = x, v = y, w = \beta_3 xy$  we notice that mirroring the structuring element by replacing  $y$  with  $-y$ , followed by replacing  $w$  with  $-w$ , restores the original function. Thus, for each minimiser  $w^*$  in this case,  $-w^*$  is also a minimiser, and by convexity of the objective function  $w^* = 0$  is a minimiser.

Regarding  $\alpha_3$  and  $\delta_3$ , notice that rotation of the structuring element by 90 degrees switches the roles of  $\alpha$  and  $\delta$ . As this rotation leaves the input value set unchanged, we see that  $\alpha_3$  and  $\delta_3$  must have equal effects. We can therefore consider the rotationally symmetric case  $\alpha_3 = \delta_3$ .

Assume therefore that we have  $u = x, v = y$ , and  $w = \alpha(x^2 + y^2)$ , and  $M = (0, 0, w^*)$  is the sought 2D Oja median. The median point constitutes an equilibrium between forces exercised by point pairs  $(A, B)$  with  $A = (u_1, v_1, w_1) = (x_1, y_1, \alpha(x_1^2 + y_1^2))$ ,  $B = (u_2, v_2, w_2) = (x_2, y_2, \alpha(x_2^2 + y_2^2))$ . The force coming from a single point pair  $(A, B)$  is expressed by a vector of length  $|AB|$  in direction  $MH$ , where  $H$  is the foot of the altitude on  $AB$  in the triangle  $MAB$ . Thus, the sought 2D Oja median is a weighted  $L^1$  median of the feet  $H$ , weighted with the base lengths  $|AB|$ . The equilibrium condition for  $M$  can therefore be written similarly as in (114) as

$$0 = \iint_{D_\varrho} \iint_{D_\varrho} \frac{MH}{|MH|} |AB| dy_2 dx_2 dy_1 dx_1 \quad (130)$$

where the points  $H, A, B$  still need to be expressed in coordinates. Before we do so, we notice that reorganisation of the quadruple integral in Radon-like polar coordinates as in Appendix A creates an additional weight factor  $|AB|$  and an integrand that is rotationally symmetric with regard to the angular coordinate  $\varphi$ . One can therefore drop the integration over  $\varphi$  and consider just  $\varphi = 0$  as minimality condition. Denoting by  $H', A', B'$  the projections of  $H, A, B$ , respectively, to the  $u$ - $v$  plane, the case  $\varphi = 0$  describes a configuration in which  $A'B'$  is aligned in  $v$  direction, and the altitude in  $MA'B'$  therefore in  $u$  direction. Since  $H'$  deviates from the foot of the altitude in  $MA'B'$  at most by higher order terms, we can

assume that  $H' = (x, 0)$ ,  $A' = (x, y_1)$ ,  $B' = (x, y_2)$ . The 3D points  $A$  and  $B$  are then given by  $A = (x, y_1, \alpha(x^2 + y_1^2))$ ,  $B = (x, y_2, \alpha(x^2 + y_2^2))$ .  $H$  is given up to higher order terms by  $H = (x, 0, \alpha(x^2 - y_1 y_2))$ .

This leads to the simplified equilibrium condition

$$0 = \int_0^\varrho \int_{-\sqrt{\varrho^2-x^2}}^{\sqrt{\varrho^2-x^2}} \int_{-\sqrt{\varrho^2-x^2}}^{\sqrt{\varrho^2-x^2}} \frac{(y_2 - y_1)^2 (\alpha(x^2 - y_1 y_2) - w^*)}{\sqrt{x^2 + (\alpha(x^2 - y_1 y_2) - w^*)^2}} dy_2 dy_1 dx, \quad (131)$$

and after substituting  $x = \xi\varrho$ ,  $y_1 = \eta_1\varrho$ ,  $y_2 = \eta_2\varrho$ ,  $w^* = \nu\varrho^2$  one has

$$0 = \int_0^1 \int_{-\sqrt{1-\xi^2}}^{\sqrt{1-\xi^2}} \int_{-\sqrt{1-\xi^2}}^{\sqrt{1-\xi^2}} \frac{(\eta_2 - \eta_1)^2 (\alpha(\xi^2 - \eta_1 \eta_2) - \nu)}{\sqrt{\xi^2 + \varrho^2 (\alpha(\xi^2 - \eta_1 \eta_2) - \nu)^2}} d\eta_2 d\eta_1 d\xi. \quad (132)$$

Splitting the integration range of the outer integral to the two intervals  $[0, \varrho^{2/3}]$  and  $[\varrho^{2/3}, 1]$  we see that the first integral yields  $\mathcal{O}(\varrho^{2/3})$  since its integrand is absolutely bounded by 1, whereas the second integral is simplified further by noticing that  $\sqrt{\xi^2 + \varrho^2 (\alpha(\xi^2 - \eta_1 \eta_2) - \nu)^2} = \xi(1 + \mathcal{O}(\varrho^{2/3}))$  to

$$0 = \int_{\varrho^{2/3}}^1 \int_{-\sqrt{1-\xi^2}}^{\sqrt{1-\xi^2}} \int_{-\sqrt{1-\xi^2}}^{\sqrt{1-\xi^2}} \frac{(\eta_2 - \eta_1)^2 (\alpha(\xi^2 - \eta_1 \eta_2) - \nu)}{\xi} d\eta_2 d\eta_1 d\xi + \mathcal{O}(\varrho^{2/3}) \quad (133)$$

from which we obtain

$$\frac{\nu}{\alpha} = \frac{\int_{\varrho^{2/3}}^1 \int_{-\sqrt{1-\xi^2}}^{\sqrt{1-\xi^2}} \int_{-\sqrt{1-\xi^2}}^{\sqrt{1-\xi^2}} (\eta_2 - \eta_1)^2 (\xi^2 - \eta_1 \eta_2) \xi^{-1} d\eta_2 d\eta_1 d\xi}{\int_{\varrho^{2/3}}^1 \int_{-\sqrt{1-\xi^2}}^{\sqrt{1-\xi^2}} \int_{-\sqrt{1-\xi^2}}^{\sqrt{1-\xi^2}} (\eta_2 - \eta_1)^2 \xi^{-1} d\eta_2 d\eta_1 d\xi} \quad (134)$$

and after integral evaluation

$$\frac{\nu}{\alpha} = \frac{-\ln \varrho \cdot 16/27 - 10/27}{-\ln \varrho \cdot 16/9 - 16/9} \xrightarrow{\varrho \rightarrow 0} \frac{1}{3}. \quad (135)$$

Since for the given function one has  $w_{xx} = w_{yy} = 2\alpha$ , it follows that each of  $w_{xx}$  and  $w_{yy}$  effects  $w^*$  with weight  $1/12$ , which concludes the proof.  $\square$

## F Numerical Scheme for the PDE (38)

We use the notations from Section 4.2.1. By square brackets  $[\dots]$  we denote discrete approximations of the enclosed derivative expressions at pixel  $(i, j)$  in time step  $k$ . The numerical scheme for the PDE (38) proceeds for each pixel  $(i, j)$  as follows.

1. Compute the central difference approximations

$$[\mathbf{u}_x] := \frac{1}{2h} (\mathbf{u}_{i+1,j}^k - \mathbf{u}_{i-1,j}^k), \quad (136)$$

$$[\mathbf{u}_y] := \frac{1}{2h} (\mathbf{u}_{i,j+1}^k - \mathbf{u}_{i,j-1}^k). \quad (137)$$

2. From  $[\mathbf{D}\mathbf{u}] = ([\mathbf{u}_x] \mid [\mathbf{u}_y])$  compute the  $3 \times 3$  tensor product matrix  $\mathbf{C} := [\mathbf{D}\mathbf{u}][\mathbf{D}\mathbf{u}]^T$ . Compute the spectral decomposition of  $\mathbf{C}$ ,

$$\mathbf{C} = \mathbf{Q}\mathbf{\Lambda}\mathbf{Q}^T \quad (138)$$

where  $\mathbf{Q}$  is orthogonal, and  $\mathbf{\Lambda}$  is the diagonal matrix of the (nonnegative) eigenvalues of  $\mathbf{C}$  in decreasing order,  $\lambda_1 \geq \lambda_2 \geq \lambda_3$ .

3. Apply to the input values  $\mathbf{u}_{i,j}^k$  the orthogonal transform

$$\hat{\mathbf{u}}_{i,j}^k := \mathbf{Q}^T \mathbf{u}_{i,j}^k . \quad (139)$$

Note that hereafter, the first and second channel of  $\hat{\mathbf{u}}$  hold the directions of dominant variation within the patch, i.e. the first two basis vectors of the transformed data set span the tangential space of the image graph. Moreover, the gradients of the first two channels of  $\hat{\mathbf{u}}$  are orthogonal in the  $(x, y)$  plane.

4. Compute the central difference approximations

$$[\hat{\mathbf{u}}_x] := \frac{1}{2h}(\hat{\mathbf{u}}_{i+1,j}^k - \hat{\mathbf{u}}_{i-1,j}^k) , \quad (140)$$

$$[\hat{\mathbf{u}}_y] := \frac{1}{2h}(\hat{\mathbf{u}}_{i,j+1}^k - \hat{\mathbf{u}}_{i,j-1}^k) , \quad (141)$$

$$[\hat{\mathbf{u}}_{xx}] := \frac{1}{h^2}(\hat{\mathbf{u}}_{i+1,j}^k - 2\hat{\mathbf{u}}_{i,j}^k + \hat{\mathbf{u}}_{i-1,j}^k) , \quad (142)$$

$$[\hat{\mathbf{u}}_{yy}] := \frac{1}{h^2}(\hat{\mathbf{u}}_{i,j+1}^k - 2\hat{\mathbf{u}}_{i,j}^k + \hat{\mathbf{u}}_{i,j-1}^k) , \quad (143)$$

$$[\hat{\mathbf{u}}_{xy}] := \frac{1}{4h^2}(\hat{\mathbf{u}}_{i+1,j+1}^k - \hat{\mathbf{u}}_{i+1,j-1}^k - \hat{\mathbf{u}}_{i-1,j+1}^k + \hat{\mathbf{u}}_{i-1,j-1}^k) . \quad (144)$$

5. Compute the first contribution to  $\hat{\mathbf{u}}_t$  as

$$\hat{\mathbf{z}}_1 := [\hat{\mathbf{u}}_{xx}] + [\hat{\mathbf{u}}_{yy}] . \quad (145)$$

6. From the first component  $\hat{u}$  of  $\hat{\mathbf{u}}$ , determine the image adaptive directions

$$\boldsymbol{\eta} := \begin{pmatrix} c \\ s \end{pmatrix} = \frac{1}{\sqrt{[\hat{u}_x]^2 + [\hat{u}_y]^2}} \begin{pmatrix} [\hat{u}_x] \\ [\hat{u}_y] \end{pmatrix} , \quad (146)$$

$$\boldsymbol{\xi} := \begin{pmatrix} -s \\ c \end{pmatrix} \quad (147)$$

and the directional derivatives

$$[\hat{\mathbf{u}}_{\boldsymbol{\eta}}] := c[\hat{\mathbf{u}}_x] + s[\hat{\mathbf{u}}_y] , \quad (148)$$

$$[\hat{\mathbf{u}}_{\boldsymbol{\xi}}] := -s[\hat{\mathbf{u}}_x] + c[\hat{\mathbf{u}}_y] , \quad (149)$$

$$[\hat{\mathbf{u}}_{\boldsymbol{\eta}\boldsymbol{\eta}}] := c^2[\hat{\mathbf{u}}_{xx}] + 2cs[\hat{\mathbf{u}}_{xy}] + s^2[\hat{\mathbf{u}}_{yy}] , \quad (150)$$

$$[\hat{\mathbf{u}}_{\boldsymbol{\xi}\boldsymbol{\xi}}] := s^2[\hat{\mathbf{u}}_{xx}] - 2cs[\hat{\mathbf{u}}_{xy}] + c^2[\hat{\mathbf{u}}_{yy}] , \quad (151)$$

$$[\hat{\mathbf{u}}_{\boldsymbol{\eta}\boldsymbol{\xi}}] := cs([\hat{\mathbf{u}}_{yy}] - [\hat{\mathbf{u}}_{xx}]) + (c^2 - s^2)[\hat{\mathbf{u}}_{xy}] . \quad (152)$$

7. Compute the second contribution to  $\hat{\mathbf{u}}_t$  as

$$\hat{\mathbf{z}}_2 := 2([\hat{\mathbf{u}}_{\boldsymbol{\xi}\boldsymbol{\xi}}], [\hat{\mathbf{u}}_{\boldsymbol{\eta}\boldsymbol{\eta}}], 0)^T . \quad (153)$$

8. Compute one-sided derivatives

$$[\hat{\mathbf{u}}_x]^+ := \frac{1}{h}(\hat{\mathbf{u}}_{i+1,j}^k - \hat{\mathbf{u}}_{i,j}^k), \quad (154)$$

$$[\hat{\mathbf{u}}_x]^- := \frac{1}{h}(\hat{\mathbf{u}}_{i,j}^k - \hat{\mathbf{u}}_{i-1,j}^k), \quad (155)$$

$$[\hat{\mathbf{u}}_y]^+ := \frac{1}{h}(\hat{\mathbf{u}}_{i,j+1}^k - \hat{\mathbf{u}}_{i,j}^k), \quad (156)$$

$$[\hat{\mathbf{u}}_y]^- := \frac{1}{h}(\hat{\mathbf{u}}_{i,j}^k - \hat{\mathbf{u}}_{i,j-1}^k). \quad (157)$$

If  $[\hat{\mathbf{u}}_x]^+$  and  $[\hat{\mathbf{u}}_x]^-$  have opposite sign, replace the one with larger absolute value with their sum  $[\hat{\mathbf{u}}_x]^+ + [\hat{\mathbf{u}}_x]^-$  and set the other one to zero (minmod stabilisation). Proceed in the same way for  $[\hat{\mathbf{u}}_y]^\pm$ . From the so obtained approximations, compute one-sided directional derivatives

$$[\hat{\mathbf{u}}_\eta]^\pm := c[\hat{\mathbf{u}}_x]^\pm + s[\hat{\mathbf{u}}_y]^\pm, \quad (158)$$

$$[\hat{\mathbf{u}}_\xi]^\pm := -s[\hat{\mathbf{u}}_x]^\mp + c[\hat{\mathbf{u}}_y]^\pm, \quad (159)$$

if  $c, s \geq 0$ , and analogously for other sign combinations of  $c, s$ .

9. Compute regularised approximations  $R_v$  for  $v_{\eta\xi}/v_\xi$  and  $R_u$  for  $u_{\eta\xi}/u_\eta$  as

$$R_v := \frac{2[\hat{v}_{\eta\xi}][\hat{v}_\xi]}{([\hat{v}_\xi]^+)^2 + ([\hat{v}_\xi]^-)^2 + 2\varepsilon}, \quad (160)$$

$$R_u := \frac{2[\hat{u}_{\eta\xi}][\hat{u}_\eta]}{([\hat{u}_\eta]^+)^2 + ([\hat{u}_\eta]^-)^2 + 2\varepsilon} \quad (161)$$

with a fixed numerical regularisation parameter  $\varepsilon$ .

10. Compute the third contribution to  $\hat{\mathbf{u}}_t$  by the upwind discretisation

$$\mathbf{z}_3 := (R_v[\hat{u}_\eta]^\mp, R_u[\hat{v}_\xi]^\mp, 0)^\top, \quad (162)$$

choosing in each component the backward approximation  $[\dots]^-$  if the preceding factor is positive, and  $[\dots]^+$  otherwise.

11. Let  $[\hat{\mathbf{u}}_t] := \mathbf{z}_1 + \mathbf{z}_2 - \mathbf{z}_3$  and by inverting the orthogonal transform

$$[\mathbf{u}_t] := \mathbf{Q} [\hat{\mathbf{u}}_t]. \quad (163)$$

12. Compute  $\mathbf{u}_{i,j}^{k+1} = \mathbf{u}_{i,j}^k + \tau[\mathbf{u}_t]$ .

## References

- [1] Aloupis, G., Langerman, S., Soss, M., Toussaint, G.: Algorithms for bivariate medians and a Fermat–Torricelli problem for lines. *Computational Geometry* **26**, 69–79 (2003)
- [2] Alvarez, L., Lions, P.L., Morel, J.M.: Image selective smoothing and edge detection by nonlinear diffusion. II. *SIAM Journal on Numerical Analysis* **29**, 845–866 (1992)
- [3] Anandan, P.: A computational framework and an algorithm for the measurement of visual motion. *International Journal of Computer Vision* **2**, 283–310 (1989)

- [4] Astola, J., Haavisto, P., Neuvo, Y.: Vector median filters. *Proceedings of the IEEE* **78**(4), 678–689 (1990)
- [5] Austin, T.L.: An approximation to the point of minimum aggregate distance. *Metron* **19**, 10–21 (1959)
- [6] Barbara, R.: The Fermat–Torricelli points of  $n$  lines. *Mathematical Gazette* **84**, 24–29 (2001)
- [7] Boris, J.P., Book, D.L.: Flux corrected transport. I. SHASTA, a fluid transport algorithm that works. *Journal of Computational Physics* **11**(1), 38–69 (1973)
- [8] Breuß, M., Brox, T., Sonar, T., Weickert, J.: Stabilised nonlinear inverse diffusion for approximating hyperbolic PDEs. In: Kimmel, R., Sochen, S., Weickert, J. (eds.) *Scale Space and PDE Methods in Computer Vision, Lecture Notes in Computer Science*, vol. 3459, pp. 536–547. Springer, Berlin (2005)
- [9] Caselles, V., Sapiro, G., Chung, D.H.: Vector median filters, inf-sup operations, and coupled PDE’s: Theoretical connections. *Journal of Mathematical Imaging and Vision* **8**, 109–119 (2000)
- [10] Chakraborty, B., Chaudhuri, P.: On a transformation and re-transformation technique for constructing an affine equivariant multivariate median. *Proceedings of the AMS* **124**(6), 2539–2547 (1996)
- [11] Chakraborty, B., Chaudhuri, P.: A note on the robustness of multivariate medians. *Statistics and Probability Letters* **45**, 269–276 (1999)
- [12] Chung, D.H., Sapiro, G.: On the level lines and geometry of vector-valued images. *IEEE Signal Processing Letters* **7**(9), 241–243 (2000)
- [13] Eckhardt, U.: Root images of median filters. *Journal of Mathematical Imaging and Vision* **19**, 63–70 (2003)
- [14] Gini, C., Galvani, L.: Di talune estensioni dei concetti di media ai caratteri qualitativi. *Metron* **8**, 3–209 (1929)
- [15] Guichard, F., Morel, J.M.: Partial differential equations and image iterative filtering. In: Duff, I.S., Watson, G.A. (eds.) *The State of the Art in Numerical Analysis*, no. 63 in IMA Conference Series (New Series), pp. 525–562. Clarendon Press, Oxford (1997)
- [16] Hayford, J.F.: What is the center of an area, or the center of a population? *Journal of the American Statistical Association* **8**(58), 47–58 (1902)
- [17] Hettmansperger, T.P., Randles, R.H.: A practical affine equivariant multivariate median. *Biometrika* **89**(4), 851–860 (2002)
- [18] Horn, B., Schunck, B.: Determining optical flow. *Artificial Intelligence* **17**, 185–203 (1981)

- [19] Kleefeld, A., Breuß, M., Welk, M., Burgeth, B.: Adaptive filters for color images: median filtering and its extensions. In: Trémeau, A., Schettini, R., Tominaga, S. (eds.) *Computational Color Imaging, Lecture Notes in Computer Science*, vol. 9016, pp. 149–158. Springer, Cham (2015)
- [20] Mémin, E., Pérez, P.: Dense estimation and object-based segmentation of the optical flow with robust techniques. *IEEE Transactions on Image Processing* **7**(5), 703–719 (1998)
- [21] Oja, H.: Descriptive statistics for multivariate distributions. *Statistics and Probability Letters* **1**, 327–332 (1983)
- [22] Rao, C.R.: Methodology based on the  $l_1$ -norm in statistical inference. *Sankhyā A* **50**, 289–313 (1988)
- [23] Ronkainen, T., Oja, H., Orponen, P.: Computation of the multivariate Oja median. In: Dutter, R., Filzmoser, P., Gather, U., Rousseeuw, P.J. (eds.) *Developments in Robust Statistics*, pp. 344–359. Physica-Verlag, Heidelberg (2003)
- [24] Small, C.G.: A survey of multidimensional medians. *International Statistical Review* **58**(3), 263–277 (1990)
- [25] Spence, C., Fancourt, C.: An iterative method for vector median filtering. In: *Proc. 2007 IEEE International Conference on Image Processing*, vol. 5, pp. 265–268 (2007)
- [26] Struyf, A., Hubert, M., Rousseeuw, P.J.: Clustering in an object-oriented environment. *Journal of Statistical Software* **1**(4), 1–30 (1997)
- [27] Tukey, J.W.: *Exploratory Data Analysis*. Addison–Wesley, Menlo Park (1971)
- [28] Vardi, Y., Zhang, C.H.: A modified Weiszfeld algorithm for the Fermat–Weber location problem. *Mathematical Programming A* **90**, 559–566 (2001)
- [29] Weber, A.: *Über den Standort der Industrien*. Mohr, Tübingen (1909)
- [30] Weiszfeld, E.: Sur le point pour lequel la somme des distances de  $n$  points donnés est minimum. *Tôhoku Mathematics Journal* **43**, 355–386 (1937)
- [31] Welk, M.: Partial differential equations for bivariate median filters. In: Aujol, J.-F., Nikolova, M., Papadakis, N. (eds.) *Scale Space and Variational Methods in Computer Vision, Lecture Notes in Computer Science*, vol. 9087, pp. 53–65. Springer, Cham (2015)
- [32] Welk, M.: Corrected PDE approximation result for the multivariate  $L^1$  median filter. Tech. rep. (In preparation)
- [33] Welk, M., Breuß, M.: Morphological amoebas and partial differential equations. In: Hawkes, P.W. (ed.) *Advances in Imaging and Electron Physics*, vol. 185, pp. 139–212. Elsevier Academic Press (2014)
- [34] Welk, M., Breuß, M., Vogel, O.: Morphological amoebas are self-snakes. *Journal of Mathematical Imaging and Vision* **39**, 87–99 (2011)
- [35] Welk, M., Feddern, C., Burgeth, B., Weickert, J.: Median filtering of tensor-valued images. In: Michaelis, B., Krell, G. (eds.) *Pattern Recognition, Lecture Notes in Computer Science*, vol. 2781, pp. 17–24. Springer, Berlin (2003)